Journal for ImmunoTherapy of Cancer

Spatial immune atlas of breast cancer brain metastasis reveals CD163$^+$ macrophage reprogramming associated with immune escape

Jiale Zhu,[1,2] Junjie Ye,[1] Yulin Ma,[1] Zhirong Lin,[1,3] Yupeng Wen,[1] Jianpeng Sheng ,[4] Mei Yang[1,5]

To cite: Zhu J, Ye J, Ma Y, *et al*. Spatial immune atlas of breast cancer brain metastasis reveals CD163$^+$ macrophage reprogramming associated with immune escape. *Journal for ImmunoTherapy of Cancer* 2026;**14**:e014421. doi:10.1136/jitc-2025-014421

► Additional supplemental material is published online only. To view, please visit the journal online (https://doi.org/10.1136/jitc-2025-014421).

JZ and JY contributed equally.

Accepted 05 June 2026

For numbered affiliations see end of article.

Correspondence to
Dr Mei Yang;
yangmei286@163.com

ABSTRACT

Background Brain metastases (BrM) remain a major cause of mortality in breast cancer (BC), yet the spatial organization and molecular circuitry of the metastatic immune microenvironment are poorly defined.

Methods To address this gap, we integrated high-plex imaging mass cytometry (IMC) performed on human primary breast tumors (n=20 regions of interests (ROIs)) and human brain-metastasis tissues (n=40 ROIs) with publicly available datasets, including single-cell RNA sequencing (scRNA-seq) from BC (n=10) and BrM (n=12) and spatial transcriptomic (ST) data from BC (n=7) and BrM (n=1), enabling single-cell resolution of tissue architecture, functional states, and intercellular signaling.

Results IMC resolved nine major cell classes and diverse epithelial, myeloid, and T-cell subtypes, and revealed a striking shift in macrophage polarization: CD163$^-$CD11b$^-$ macrophages were markedly depleted in brain metastases, whereas CD163$^+$ subsets persisted. Spatial analysis demonstrated the loss of the immune-permissive CN1 neighborhood in brain metastases, which is enriched in memory T cells, B cells, and dendritic cells, and the expansion of the immunosuppressive CN9 niche in brain metastases, containing CD163$^+$ macrophages, invasion-like epithelial cells, and exhausted T cells. ScRNA-seq integration corroborated these findings by refining the annotation of major immune and stromal lineages and confirming CD163 expression patterns across macrophage subsets. ST deconvolution further reproduced these CN1-like and CN9-like domains in situ, validating their anatomical organization across BC and BrM. Ligand-receptor inference highlighted specific inhibitory pathways—including programmed cell death protein 1/programmed death-ligand 1, growth arrest-specific 6-Tyro3, Axl, and Mer receptor tyrosine kinase family, nectin cell adhesion molecule 2 (NECTIN2)-T-cell immunoreceptor with Ig and ITIM domains, and prostaglandin E2 (PGE2)-prostaglandin E2 receptor 4—that are associated with immune evasion and metastatic growth. Functional validation in an in vivo brain metastasis model further supported the therapeutic relevance of targeting these immunoregulatory pathways.

Conclusions Together, these findings show a shift from permissive to suppressive immune niches, accompanied by pronounced macrophage reprogramming, as central features of BC adaptation to the brain. This spatially resolved framework provides mechanistic insight into the poor responsiveness of brain metastases to current immunotherapies and identifies defined inhibitory ligand-receptor axes as actionable targets for combination immunotherapy.

WHAT IS ALREADY KNOWN ON THIS TOPIC

⇒ Brain metastases are a major cause of mortality in breast cancer and often show limited responsiveness to immunotherapy. Although recent single-cell and transcriptomic studies have revealed cellular heterogeneity in breast cancer brain metastases, the spatial organization of the metastatic immune microenvironment and the immunoregulatory interactions that drive immune escape remain poorly defined.

WHAT THIS STUDY ADDS

⇒ This integrated spatial multi-omics study shows that breast cancer brain metastases undergo a progressive transition from an immune-permissive niche to an invasion-immunosuppressive niche, with spatial remodeling of macrophage states marked by depletion of CD163$^-$CD11b$^-$ macrophages and retention of CD163$^+$ macrophages in suppressive metastatic regions.

HOW THIS STUDY MIGHT AFFECT RESEARCH, PRACTICE OR POLICY

⇒ These findings provide a spatially resolved framework for understanding immune escape in breast cancer brain metastases and support the development of rational combination immunotherapy strategies aimed at disrupting suppressive niche programs, including the growth arrest-specific 6-Tyro3, Axl, and Mer receptor tyrosine kinase family and cluster of differentiation 47 (CD47)-signal regulatory protein alpha (SIRPA) axes, to remodel metastatic ecosystems and restore effective antitumor immunity.

BACKGROUND

Breast cancer (BC) is the most frequently diagnosed malignancy among women and

remains a leading cause of cancer-related mortality worldwide.[1] Recent GLOBOCAN estimates report more than 2.3 million new cases in 2020, surpassing lung cancer as the most commonly diagnosed cancer.[2] Despite substantial advances in surgery, radiotherapy, systemic chemotherapy, and targeted therapies, the development of distant metastasis remains the primary cause of BC mortality, with a 5-year survival of approximately 29% for metastatic disease.[3] Among the various metastatic sites, the central nervous system (CNS) poses a unique and particularly lethal challenge.[4] Brain metastases (BrM) occur in roughly 10–30% of all patients with metastatic BC, and the incidence climbs to 30–50% in human epidermal growth factor receptor 2 (HER2)-positive and triple-negative subtypes.[5 6] Median overall survival (OS) after diagnosis of brain metastasis is often well under 1 year; for example, Eichler *et al* reported a median OS of 8.3 months, and other series following stereotactic radiosurgery or HER2-targeted therapies report survival ranging from 4.5 to 14 months.[7] Therapeutic efficacy is constrained by the blood-brain barrier, the specialized neurovascular unit, and the distinct immune microenvironment of the brain, which together form a sanctuary for tumor cells that impedes drug delivery and limits immune surveillance.[8–10] Understanding how disseminated BC cells adapt to and reshape this microenvironment is therefore a critical unmet need.

Molecular profiling efforts over the past decade have illuminated key oncogenic drivers of BC progression, but bulk genomic or transcriptomic analyses obscure the cellular heterogeneity and spatial relationships that govern metastatic colonization of the brain.[11 12] Single-cell RNA sequencing (scRNA-seq) has begun to reveal the diversity of tumor, immune, and stromal populations in both primary and metastatic lesions, yet it cannot capture the precise spatial organization or direct cell–cell interactions within intact tissue.[13] Conventional histology and immunohistochemistry, while preserving spatial context, are limited to a handful of markers and cannot resolve the multiplexed molecular programs active in the tumor microenvironment.[14] Recent spatial multi-omics technologies overcome these limitations. Imaging mass cytometry (IMC) enables simultaneous detection of dozens of proteins at subcellular resolution on formalin-fixed sections, while high-resolution spatial transcriptomics platforms such as 10x Genomics Visium provide unbiased, genome-wide gene expression data directly within tissue architecture.[15] Integration of these approaches with public scRNA-seq references allows the construction of single-cell-level atlases that define cellular neighborhoods, uncover ligand-receptor signaling networks, and identify molecular pathways driving immune evasion and metastatic growth.[16]

In the present study, we applied a comprehensive spatial multi-omics strategy to BC BrM. Using a 39-plex IMC antibody panel, public scRNA-seq datasets, and high-resolution spatial transcriptomics (ST), we systematically mapped the cellular composition, spatial organization, and intercellular communication within metastatic lesions. This integrative framework enables identification of distinct cellular neighborhoods, characterization of key tumor-immune and stromal interactions, and discovery of signaling pathways that may underlie tumor adaptation to the brain metastatic niche. In addition, in vivo therapeutic experiments combined with histopathological and multiplex immunohistochemistry (mIHC) analyses were performed to further assess the functional relevance of targeting key immunoregulatory pathways in BC brain metastasis. Our findings provide a high-resolution atlas of the BC brain metastatic microenvironment and highlight potential targets for therapeutic intervention.

RESULTS

Multi-omics workflow and IMC panel design

We established a multi-omics framework to dissect ecosystems across breast primary (BC) and BrM. IMC was performed on 60 regions of interest (ROIs: 20 BC, 40 BrM), followed by integration with publicly available scRNA-seq (BC: n=10; BrM: n=12) and ST datasets (BC: n=7; BrM: n=1) to connect protein-level spatial states with transcriptional programs and regulatory signaling (figure 1A). The analysis workflow included IMC image acquisition and segmentation, single-cell phenotyping, spatial neighborhood analysis, scRNA-seq-based cell-state annotation, and ST-based spatial deconvolution with downstream regulatory inference. To further assess the functional relevance of the identified immunoregulatory programs, a 4T1-Luc brain metastasis mouse model was established for in vivo treatment and validation.

To capture epithelial states, immune polarization, stromal-vascular architecture, and immune checkpoints relevant to metastatic adaptation, we designed a 39-antibody IMC panel spanning tissue structure, myeloid/lymphoid, and functional markers (figure 1B). Structure markers included Pan-cytokeratin, CK7, CK8, E-cadherin, collagen I, αSMA, Vimentin, and CD31, plus CNS-lineage markers (eg, P2Y12, GFAP, Olig2, NeuN) to profile brain-resident compartments in BrM. Myeloid/lymphoid markers (CD45, CD16, CD14, CD11b, CD11c, CD68, CD163, CD3, CD4, CD8, CD20, FoxP3, CCR7, CD57) enabled resolution of macrophage states ($CD163^{\pm}$, $PD\text{-}L1^{+}$) and T-cell activation/exhaustion phenotypes. Functional markers (S100A9, (fibroblast activation protein) FAP, cleaved caspase-3, podoplanin (PDPN), indoleamine 2,3-dioxygenase 1 (IDO-1), programmed death-ligand 1 (PD-L1), programmed cell death protein 1 (PD-1), granzyme B, marker of proliferation (Ki-67), human leukocyte antigen DR (HLA-DR), sex-determining region Y-box 2 (SOX2), matrix metalloproteinase (MMP)9) were selected to distinguish proliferating, apoptotic, immune checkpoint-expressing, antigen-presenting, invasive, and stemness-associated cell

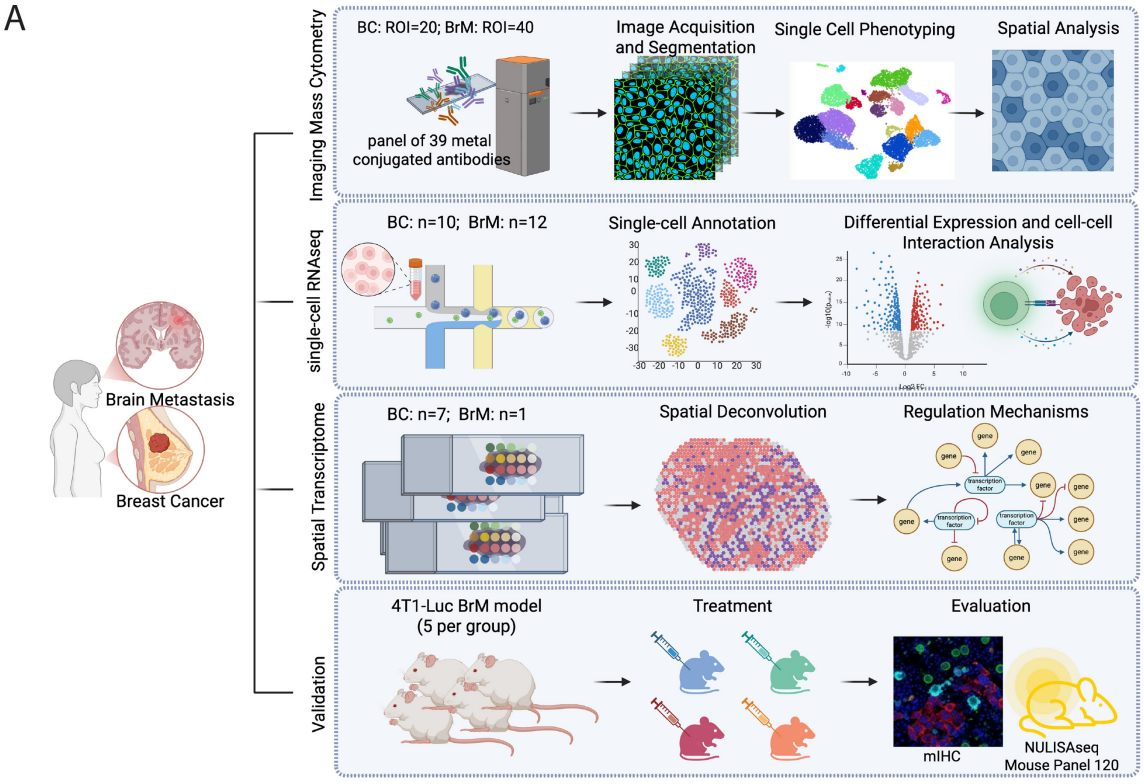

B

Panel Design			
Tissue structures	Pan-cytokeratin	Lymphoid	CD3
	CK7		CD4
	CK8		CD8
	E-cadherin		FoxP3
	P2Y12		CCR7
	GFAP		CD20
	Olig2		CD57
	NeuN	Function-related	S100A9
	CollagenI		FAP
	aSMA		cleavedCaspase-3
	Vimentin		PDPN
	CD31		IDO-1
Myeloid	CD45		PD-L1
	CD16		PD-1
	CD14		GranzymeB
	CD11b		Ki-67
	CD163		HLA-DR
	CD68		SOX2
	CD11c		MMP9

C

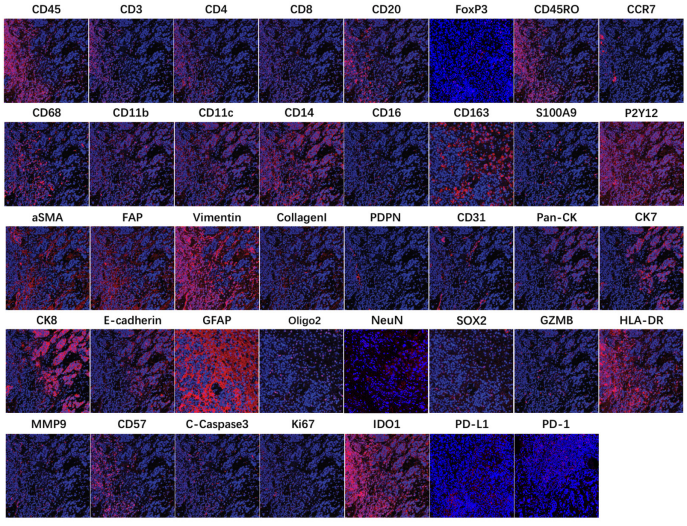

Figure 1 Integrated spatial multi-omics workflow and antibody panel for breast cancer and brain metastases. (A) Experimental design integrating IMC, public single-cell RNA sequencing, spatial transcriptomics, and in vivo validation for analysis of primary breast cancer and brain metastases. IMC was performed on formalin-fixed paraffin-embedded sections with 20 ROIs from primary breast tumors and 40 ROIs from brain metastases. A 4T1-Luc brain metastasis mouse model was used for treatment and validation. (B) 39-plex metal-conjugated antibody panel grouped by function. Markers are organized into categories for tissue structure, immune lineage, and functional readouts. (C) Representative IMC single-channel images for structural, immune, and functional markers with nuclear counterstain (blue). Each single-channel image was selected from the most informative ROI for that marker; different markers may therefore be shown from different ROIs. BC, breast cancer; BrM, brain metastases; IMC, imaging mass cytometry; mIHC, multiplex immunohistochemistry; ROI, regions of interest.

states across multiple immune, stromal, and epithelial populations.

Representative single-channel IMC images demonstrated specific cellular localization and coherent tissue morphology across ROIs, supporting robust antibody performance and acquisition stability (figure 1C). Membrane and nuclear markers exhibited expected spatial patterns, and extracellular matrix channels delineated stromal tracts and perivascular territories, facilitating high-confidence segmentation and quantitative cell-level intensity extraction. Visual inspection of raw channels and overlays confirmed that all markers

retained expected spatial contexts. This technical foundation enabled robust downstream clustering, annotation, neighborhood-based spatial modeling, and multi-omics (IMC–scRNA-seq–ST) mechanistic analyses.

Comprehensive spatial characterization of the BC and BrM ecosystem at single-cell resolution

We profiled the cellular landscape across BC and BrM using IMC at single-cell resolution and established a reproducible annotation scheme informed by recent comprehensive spatial ecosystem studies in oncology.[17 18] After preprocessing and batch harmonization, cells were embedded and clustered in an unsupervised manner, yielding a robust set of major classes that was stable across downsampling and ROI resampling. The atlas resolved epithelial, stromal (myofibroblast, collagen I-fibroblast, mesenchymal), endothelial, myeloid, and lymphoid (T and B cell) compartments, alongside astrocytes (figure 2A).

Marker overlays validated these annotations. Epithelial cells were defined by Pan-cytokeratin, E-cadherin, and CK7/CK8. Myeloid cells were anchored by CD68 and CD14.[19] T cells were $CD3^+$ and $CD45^+$, and B cells were $CD20^+$.[20] Endothelial cells were $CD31^+$ with vessel-lining morphology.[21] Fibroblast/mesenchymal cells were αSMA^+ and/or Vimentin high, frequently aligned with collagen I tracts.[22] Astrocytes were identified by expression of the canonical glial marker GFAP.[23] Marker overlays in the embedded space recapitulated these identities, and cluster-wise mean expression heatmaps further validated lineage coherence and functional repertoire (figure 2B,C).

Subtype decomposition further resolved key functional heterogeneity. Among T cells, we identified $CD45RO^+$ CD4 T, $FoxP3^+$ Treg, $PD\text{-}1^+$ exhausted CD4 T, and $CD45RO^+$ CD8 T (figure 2D). Epithelial states included E-$cadherin^+$ epithelial, E-$cadherin^-$ epithelial-mesenchymal transition-like, cleaved $caspase\text{-}3^+$, $MMP9^+$ invasion-like, $SOX2^+$ stemness-like, $Ki\text{-}67^+$ proliferative, and $HLA\text{-}DR^+$ epithelial (figure 2E). Myeloid states encompassed $CD163^-CD11b^-$ macrophages, $CD163^+$ macrophages, $MMP9^+$ macrophages, $S100A9^+$ inflammatory macrophages, $PD\text{-}L1^+$ macrophages, dendritic cells (DC) ($CD11c^+$ $HLA\text{-}DR^+$), microglia and monocytes (figure 2F).

Spatial plausibility was confirmed by comparing raw IMC fields with annotated reconstructions, showing concordant localization of epithelial nests, perivascular endothelium, stromal tracts, and immune aggregates (figure 2G). Cross-site composition profiling revealed significant differences between BC and BrM across major classes and selected subtypes (figure 2H–J), setting the stage for neighborhood-level spatial remodeling analyses.

$CD163^-CD11b^-$ macrophages represent a phenotypically distinct subset defined by low CD163 and CD11b expression, whose functional roles remain to be fully characterized, in contrast to their $CD163^+$ counterparts which are more immunosuppressive.[24 25] In our analysis, comparative composition analysis revealed site-specific remodeling between BC and BrM across both major classes (figure 2J, online supplemental figure S1). Notably, BrM showed a relative decrease in $CD163^-$ $CD11b^-$ macrophages (p=0.0067) and $MMP9^+$ macrophages (p=0.022). E-$cadherin^+$ epithelial (p=0.029), myofibroblast (p=0.039), and mesenchymal (p=0.047) cells also exhibited a downward trend in brain metastasis tissues, compared with BC tissues (online supplemental figure S1). Sensitivity and patient-level paired analyses yielded directional trends consistent with the ROI-level analyses and are summarized in online supplemental figure S4.

Furthermore, we compared the variation of different cell types across tumor subtypes: $HER2^+$, luminal B (LB), and triple-negative breast cancer (TNBC). Notably, compared with $HER2^+$, E-$cadherin^+$ epithelial and mesenchymal cells were significantly increased in TNBC (online supplemental figure S2A). These organized, spatially coherent differences motivated subsequent neighborhood-level modeling to interrogate local interaction architectures underlying the BC-to-BrM transition.

Cell neighborhood architecture and site-specific remodeling between BC and BrM

We evaluated spatial organization by identifying cell neighborhoods (CNs) through unsupervised compositional clustering of the 10 nearest cells around each cell on IMC maps (figure 3A). Using k-means clustering on the compositional data, we defined 10 distinct CNs (figure 3B). CN1 (immune-permissive niche) mainly comprised $CD163^-CD11b^-$ macrophages along with T and B lymphocytes (such as $CD45RO^+$ CD4 T, $CD45RO^+$ CD8 T, and B cells), indicating an immune-infiltrated environment that is less immunosuppressive and suitable for antigen presentation. CN2 (mesenchymal-enriched niche) was rich in mesenchymal cells, while CN3 ($HLA\text{-}DR^+$ epithelial-enriched niche), CN8 (E-$cadherin^+$ epithelial-enriched niche), and CN10 (E-$cadherin^-$ epithelial-enriched niche) contained various epithelial cell types. CN4 (myofibroblast-enriched niche) was characterized by myofibroblasts, and CN5 ($MMP9^+$ Mϕ-vascular niche)/CN6 (monocyte-enriched niche) consisted of myeloid-enriched structures. CN9 (invasion-immunosuppression niche) included epithelial cells with invasion and stemness markers ($MMP9^+$ epithelial, $SOX2^+$ epithelial) and was associated with $CD163^+$ and $PD\text{-}L1^+$ immunosuppressive macrophages and exhausted T cells ($PD\text{-}1^+$ CD4 T and regulatory T cell (Treg)), highlighting an immune-checkpoint-high, invasive niche. Comparing CN prevalence in BC and BrM revealed CN1 (p=0.015) and CN4 (p=0.026) were more common in BC, while CN9 (p=0.033) was increased in BrM, suggesting CN1 as an immune gate that may restrict dissemination, and CN9 as a metastasis-favorable domain involved in adhesion and immune suppression (figure 3C, online supplemental figure S1B). IMC raw images correspond with the Voronoi CN maps, confirming in situ localization of cell

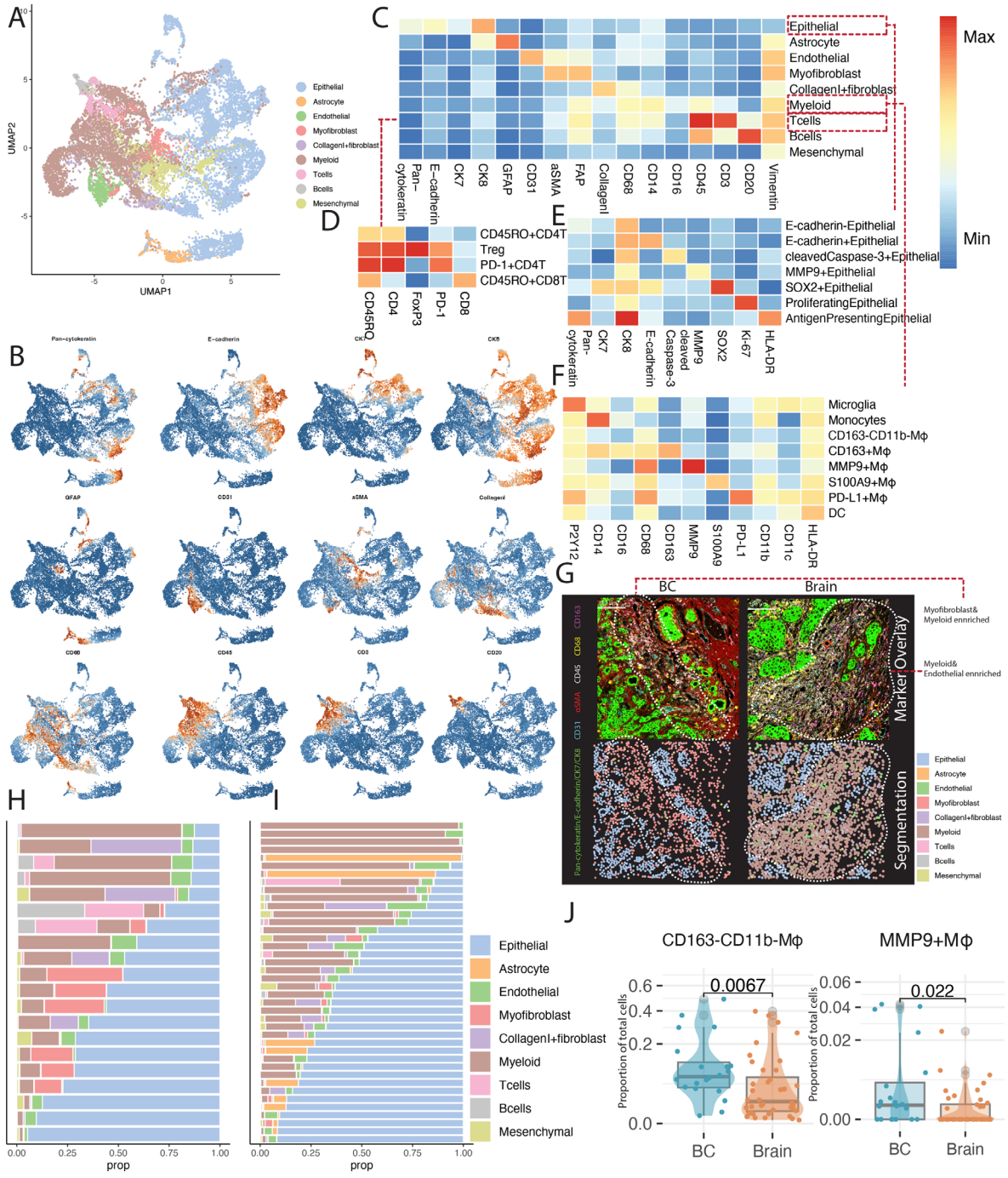

Figure 2 Imaging mass cytometry identifies major cell classes and subtypes in primary BC and BrM. (A) UMAP plot of all IMC single-cell profiles. Each color represents a major cell class: epithelial, astrocyte, endothelial, myofibroblast, collagen I^{+} fibroblast, myeloid, T cell, B cell, and mesenchymal. (B) Global UMAP overlays of representative lineage and functional markers used for cluster annotation. Each panel shows the intensity distribution of a single marker over the UMAP embedding to validate cluster identity. (C) Heatmap of marker expression across different cell populations. Colors represent scaled expression levels of the indicated markers. (D–F) Heatmap of key markers across clusters with higher-resolution subclustering of epithelial, myeloid, and T-cell compartments. Colors represent scaled expression levels of the indicated markers. (G) Representative multiplex IMC images of BC and BrM tissues (top) and corresponding annotated segmentations (bottom). Raw channels include Pan-cytokeratin/E-cadherin/CK7/CK8 (green), CD163 (purple), CD68 (yellow), CD45 (white), αSMA (red), and CD31 (blue). Annotated maps color each segmented cell by lineage assignment matching the UMAP classes in (A). Representative regions are highlighted with dotted lines to guide interpretation. (H) Stacked bar plot showing the overall distribution and proportional composition of all annotated cell types for each ROI from primary BC (20 ROIs). (I) Stacked bar plot showing the overall distribution and proportional composition of all annotated cell types for each ROI from BrM (40 ROIs). (J) Box plots comparing the ROI-level proportions of CD163^{-}CD11b^{-} macrophages and MMP9^{+} macrophages between BC and BrM. BC, breast cancer; BrM, brain metastases; IMC, imaging mass cytometry; MMP, matrix metalloproteinase; ROI, regions of interest; UMAP, Uniform Manifold Approximation and Projection.

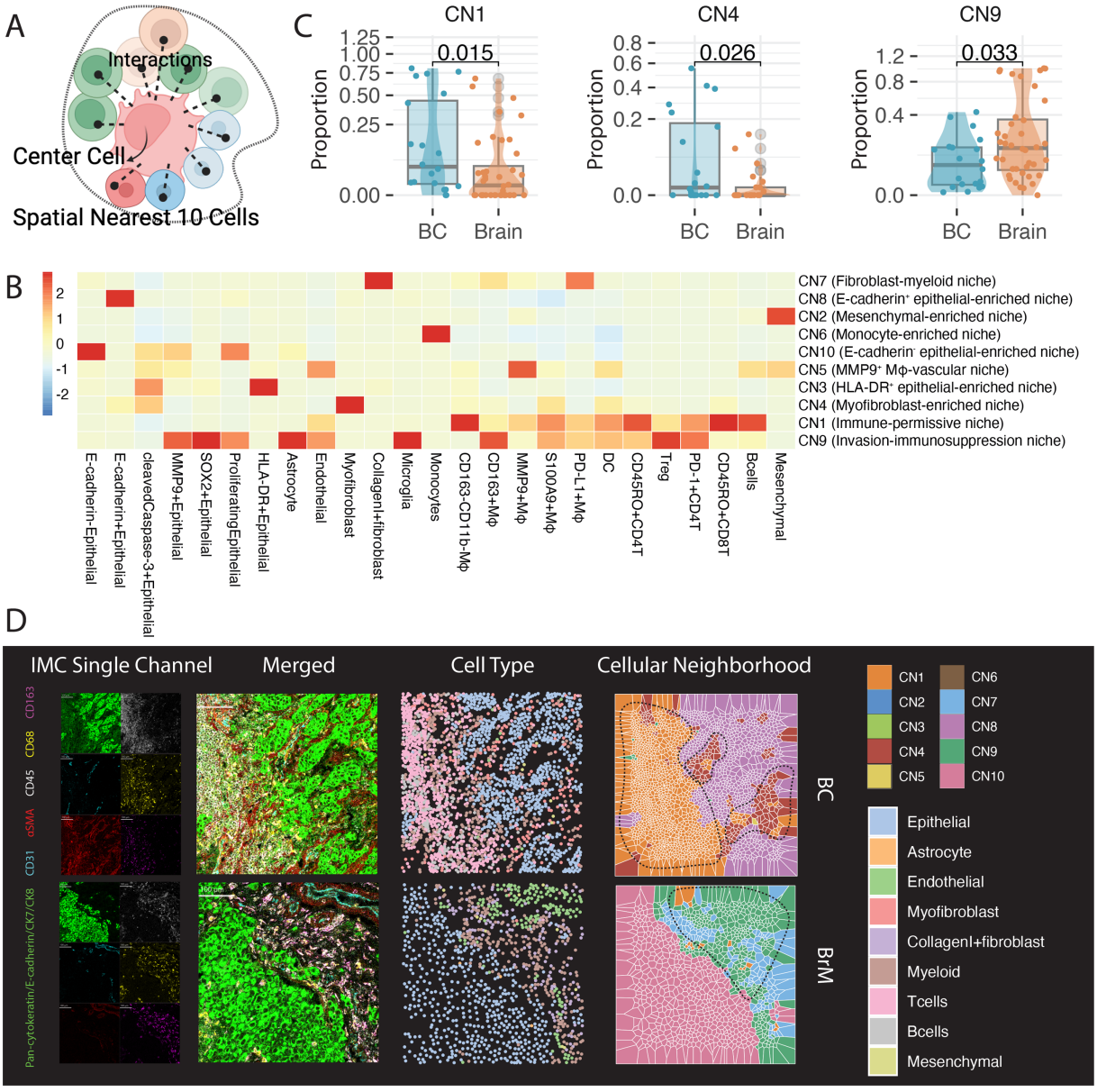

Figure 3 Spatial neighborhood identification and comparison between primary BC and BrM. (A) Definition of cellular neighborhood. Each index cell and its 10 nearest spatial neighbors are used to define a local interaction unit for compositional clustering. (B) Cellular composition of identified CNs. Column-scaled heatmap (z-score) displaying the relative enrichment of major cell types within each of the 10 cellular neighborhoods, with descriptive names assigned based on dominant compositional features. (C) Quantification of CN abundance between BC and BrM. Box plots showing ROI-level frequencies of CN1 (immune-permissive niche), CN4 (myofibroblast-enriched niche), and CN9 (invasion-immunosuppression niche) in primary BC and BrM samples, with p values indicating statistical comparisons. (D) Representative spatial mapping of CN1, CN4, and CN9 in BC and BrM. For each CN, IMC single-channel images, merged overlays, cell-type segmentation, and Voronoi-based CN maps are shown side by side. Rows are labeled BC (top) and BrM (bottom), with dotted lines highlighting the corresponding CN region. BC, breast cancer; BrM, brain metastases; CN, cell neighborhood; IMC, imaging mass cytometry; ROI, regions of interest.

types and CN boundaries (figure 3D). Furthermore, we compared the variation of CNs across tumor subtypes (HER2$^+$, LB, and TNBC). Notably, compared with HER2$^+$, CN5 was significantly decreased in TNBC, while CN10 showed a significant increase in TNBC (online supplemental figure S1B).

Our analysis of CNs in BC and BrM revealed distinct microenvironments associated with tumor progression. CN1, enriched in immune cells, likely serves as a protective immune gate in BC, while CN9, associated with invasive and immunosuppressive markers, is more prevalent in BrM, suggesting it promotes metastasis. Additionally, tumor subtype-specific differences were observed, with TNBC showing a significant reduction in CN5 and an increase in CN10 compared with HER2$^+$, indicating that these CNs may play key roles in the more aggressive and immune-evasive nature of TNBC.

Invasion-immunosuppression domain expands in BrM and rewires cell–cell interactions

Observed-to-expected ratio (Ro/e) analysis showed that CN9 undergoes site-specific remodeling. In BrM, CN9 was mainly enriched with exhausted T-cell programs, including Treg and stem-like epithelial states, whereas in BC, CN9 was mostly populated by invasive epithelial states, such as MMP9$^+$ epithelial cells (figure 4A). Cell–cell interaction analysis within CN9 revealed enhanced crosstalk among CD163$^+$ and PD-L1$^+$ macrophages and exhausted T-cell subsets. Center-neighbor aggregation showed increased spatial co-localization between PD-1$^+$ CD4 T cells and Tregs (figure 4B, online supplemental figure S3). The differential interaction analysis comparing BC and BrM highlighted increased suppressive immune interactions in BrM CN9. Positive changes in BrM were mainly observed in connections between CD163$^+$/PD-L1$^+$ macrophages and PD-1$^+$ CD4 T cells/Tregs, while BC showed relative increases in epithelial-centered interactions involving MMP9$^+$ epithelial cells (figure 4C). These patterns align with a BrM-specific shift toward immune-suppressive microcircuits within CN9.

Density-versus-distance-to-border analyses revealed distinct CN9 perimeter structures across sites. In BC, MMP9$^+$ epithelial peaks at CN9 borders, indicating an invasion-front arrangement (figure 4D). In BrM, border regions are instead mainly occupied by Treg and PD-1$^+$ CD4 T, forming a barrier-like, immune-shielded rim (figure 4E). Overall, these spatial gradients suggest a shift from an epithelial invasion-front in BC to an immunosuppressive perimeter in BrM within CN9.

Our analysis revealed that CN9 undergoes site-specific remodeling in BrM, with a shift from an invasion-driven epithelial state in BC to a more immune-suppressive environment in BrM. In BrM, CN9 is enriched with exhausted T cells and CD163$^+$ and PD-L1$^+$ macrophages, forming a protective immune barrier, while BC features more epithelial-driven invasive interactions. These findings highlight the dynamic reorganization of cell–cell interactions within CN9, with BrM adopting immune-suppressive microcircuits that may promote metastasis.

The immune-permissive/antigen-presentation niche collapses in BrM

Ro/e profiling showed that CN1 in primary BC is enriched with adaptive immune cells, including higher levels of memory T cells (CD45RO$^+$ CD4 T and CD45RO$^+$ CD8 T) and B cells. In contrast, these populations are significantly reduced in BrM CN1. Similarly, antigen-presenting signatures (DCs) associated with immune-permissive environments in BC CN1 are diminished in BrM, suggesting a loss of local antigen processing and T-B cell support within the CN1 region (figure 4F).

Cell–cell interaction analysis within CN1 highlights strong cooperative immune groups in BC, connecting memory T cells, B cells, and CD163$^-$CD11b$^-$ macrophages, with further links to DCs. These interactions suggest intact antigen presentation and lymphocyte help/effector maturation pathways (figure 4G). Differential interaction matrices reveal a widespread reduction of cooperative immune networks in BrM CN1 compared with BC, with losses in T-B and T-macrophage (CD163$^-$CD11b$^-$) interactions. This change indicates a collapse of antigen processing and helper-effector maturation within CN1 in BrM, matching the decreased presence of memory T cells, B cells, and antigen-presenting activity in this niche (figure 4H).

CN1, an immune-permissive niche in primary BC, is markedly disrupted in BrM. The reduction of memory T cells, B cells, and DCs, along with weakened T-B and T-macrophage interactions, indicates a collapse of local antigen presentation and adaptive immune coordination. This loss of immune-supportive architecture suggests that BrM progression involves dismantling of antigen-presenting niches that normally sustain effective anti-tumor immunity.

Single-cell and spatial transcriptomics contextualize CN1/CN9 biology and map IMC states to transcriptomic programs

ScRNA-seq delineated the principal tissue compartments and refined lineage-specific marker sets that anchor the IMC-defined phenotypes. A lineage marker dot-plot highlighted canonical genes separating epithelial (KRT8, KRT18), T/NK (PTPRC, CD3E, GNLY), smooth muscle cells (ACTA2), plasma B (SDC1, CD79A), pericyte (RGS5), neural (TUBB3), myeloid (CD68), endothelial (CLDN5, PECAM1), fibroblast (COL1A1, COL1A2), B (CD79A), and oligodendrocyte lineages (OLIG1, OLIG2) (figure 5A,B). Within the epithelial compartment, subprograms corresponding to invasion and stemness were resolved: an invasion$^+$ state (marked by MAPK1 and AKT1) aligning with IMC MMP9$^+$ epithelial and a stemness$^+$ state (marked by KLF4, MYC, CTNNB1, and CD44) aligning with IMC SOX2$^+$ epithelial (figure 5C,D), corroborating the CN9 association with invasive/stem-like epithelial features observed by IMC. T/natural killer (NK) differentiation included CD4$^+$ central memory (CD4$^+$), CD8$^+$ effector/memory (CD8$^+$), exhausted CD4$^+$/CD8$^+$ (CD4$^+$ Tex/CD8$^+$ Tex), Tregs, and NK cells, providing transcriptional anchors for IMC PD-1$^+$ T and Treg phenotypes. Myeloid heterogeneity was partitioned into macrophage subsets and related mononuclear phagocytes, including FOLR2$^+$, C1QC$^+$, FCN1$^+$, SPP1$^+$, APOE$^+$, CXCL10$^+$, and proliferating macrophages, plus DCs, monocytes and microglia (figure 5G,H). Mapping IMC CD163 phenotypes onto scRNA-seq clusters indicated that APOE$^+$ macrophages correspond to the CD163$^-$CD11b$^-$ subset, whereas other macrophage programs (eg, C1QC$^+$, SPP1$^+$, FOLR2$^+$, FCN1$^+$ and CXCL10$^+$) are CD163$^+$ biased, consistent with IMC-resolved CD163$^-$CD11b$^-$ Mϕ versus CD163$^+$ Mϕ compartments (figure 5I). Together, these single-cell definitions validate the IMC marker taxonomy and supply transcriptomic labels for downstream spatial deconvolution.

Using the scRNA-seq atlas as reference, we applied Robust Cell Type Decomposition (RCTD) to spatial

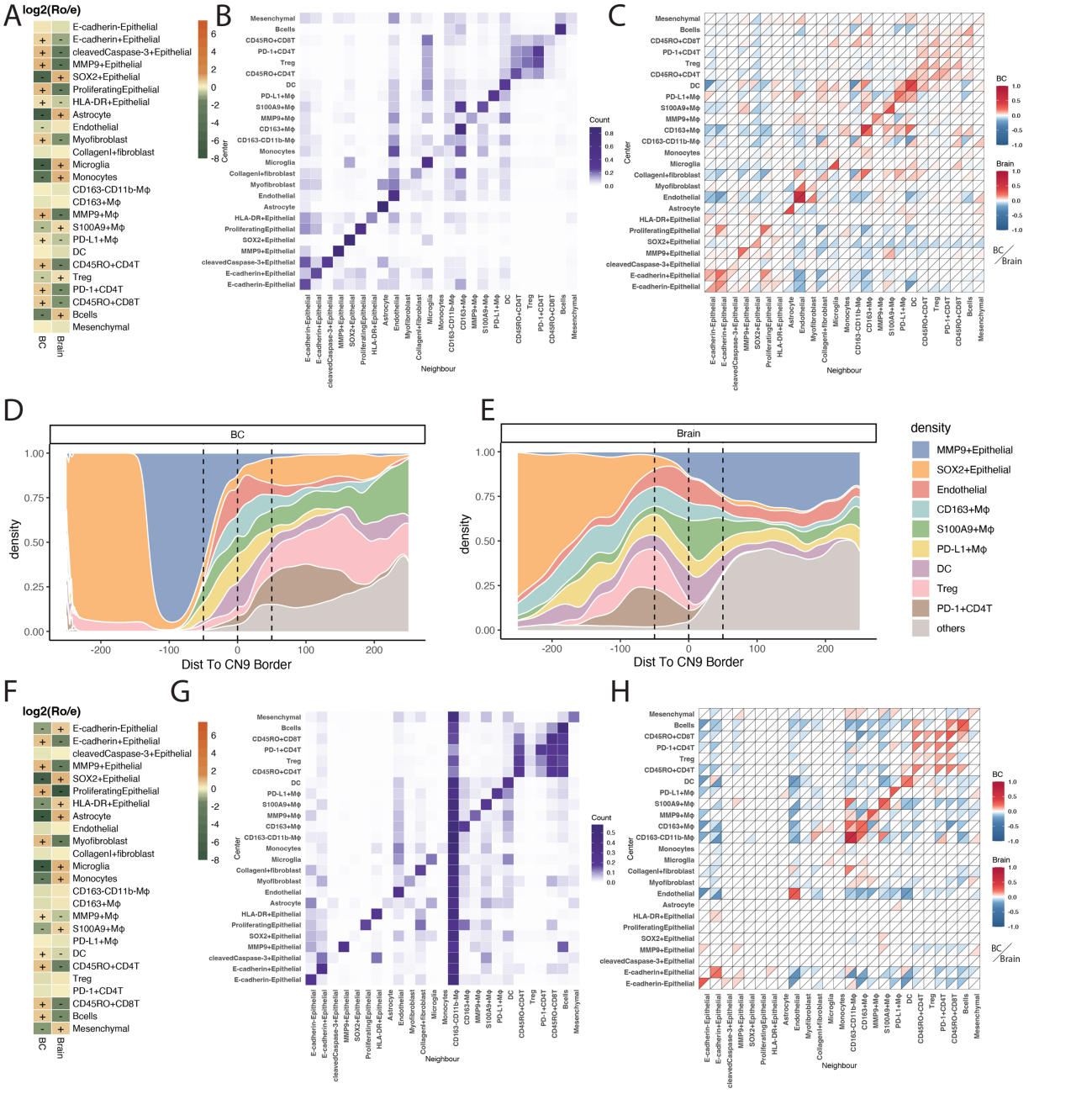

Figure 4 Spatial remodeling and interaction analysis of the CN9 invasion-immunosuppression and CN1 immune-permissive domain in BC and BrM. (A) Relative enrichment analysis of CN9 components. Log_2 (Ro/e) heatmap showing the enrichment of epithelial, myeloid, endothelial, and T-cell subsets within CN9 across BC and BrM samples. (B) Center-neighbor interaction frequencies of CN9. Heatmap showing pairwise spatial contact probabilities among key cell subsets within CN9. (C) Spatial interaction analysis within CN9. Differential split-tile interaction comparison between BC (upper-left triangle) and BrM (lower-right triangle). Color scale: red, spatial attraction; blue, avoidance. (D) CN9 border composition in primary breast cancer. Density plot showing the spatial distribution of key epithelial, myeloid, and T-cell subsets relative to the CN9 boundary in BC regions. Vertical dotted lines at –50, 0, and +50 µm demarcate the inner rim, boundary, and outer rim. (E) CN9 border composition in brain metastasis. Density plot showing the spatial arrangement of dominant immune and epithelial subsets relative to the CN9 boundary in BrM. (F) Relative enrichment of CN1 components. Log_2 (Ro/e) heatmap showing the distribution of major epithelial, myeloid, and lymphoid subsets within CN1 across BC and BrM cohorts. (G) Center-neighbor interaction frequencies of CN1. Heatmap showing pairwise spatial contact probabilities among key cell subsets within CN1. (H) Spatial interaction analysis within CN1. Differential split-tile interaction comparison between BC (upper-left triangle) and BrM (lower-right triangle). Color scale: red, spatial attraction; blue, avoidance. BC, breast cancer; BrM, brain metastases; CN, cell neighborhood; DC, dendritic cell; MMP, matrix metalloproteinase; PD-1, programmed cell death protein 1; PD-L1, programmed death-ligand 1; Ro/e, observed-to-expected ratio; Treg, regulatory T cell.

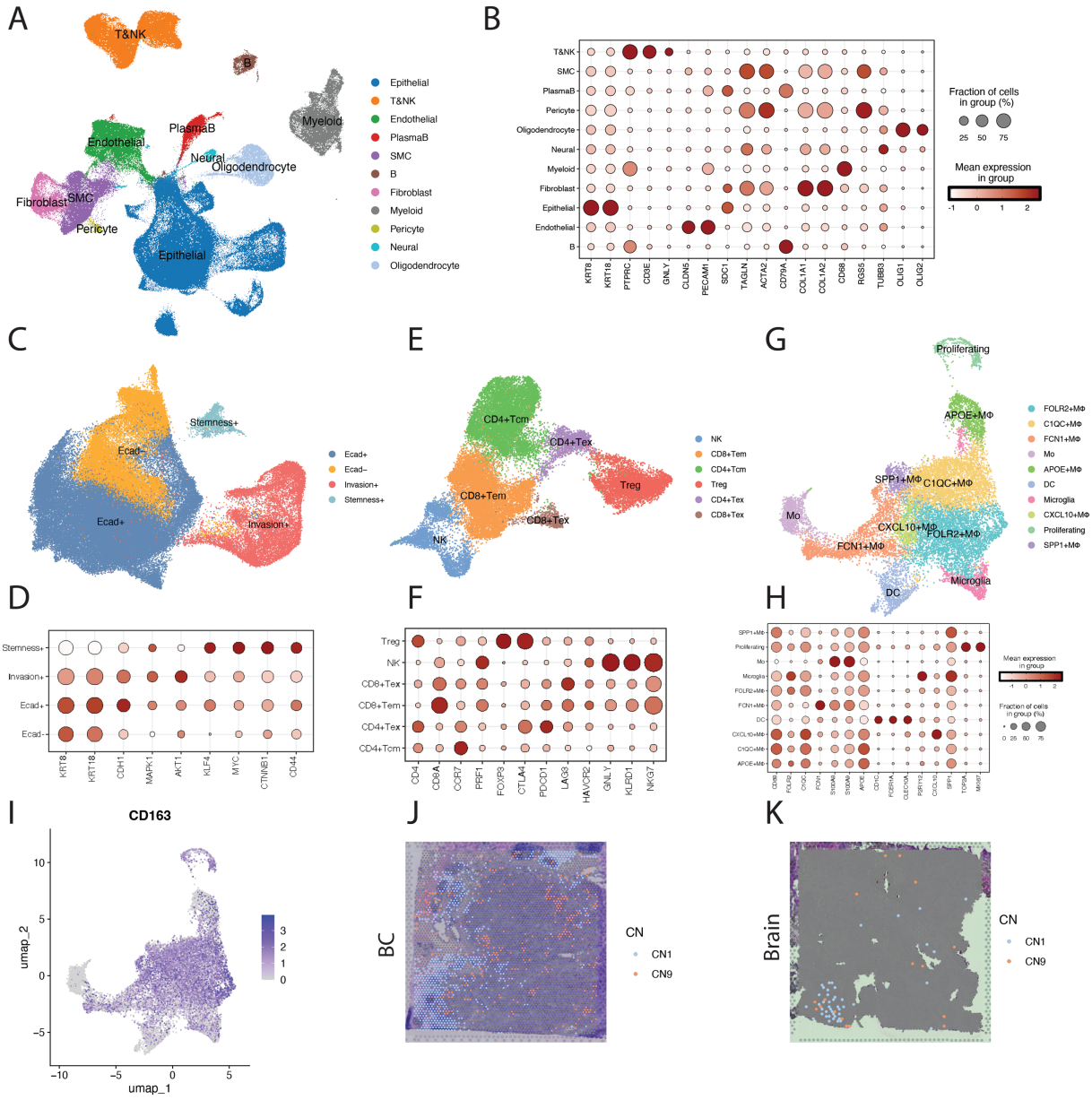

Figure 5 Integration of single-cell and spatial transcriptomics defines the transcriptional programs underlying CN1 and CN9. (A) Global single-cell landscape. UMAP visualization of single-cell RNA sequencing data showing the distribution of major tissue compartments, including epithelial, immune, stromal, and neural lineages. (B) Lineage marker expression. Dot plot displaying canonical marker genes distinguishing each major lineage, with dot size indicating the fraction of expressing cells and color representing mean expression level. (C) Epithelial subclusters. UMAP plot showing epithelial subsets characterized by E-cadherin-positive, invasion-associated, and stemness-associated transcriptional programs. (D) Epithelial gene signatures. Dot plot highlighting marker genes for invasion-related (MAPK1, AKT1) and stemness-related (KLF4, MYC, CTNNB1, CD44) epithelial states. (E) T and NK cell differentiation states. UMAP projection displaying $CD4^+$ and $CD8^+$ T-cell subsets, including effector, memory, exhausted, and regulatory populations, together with NK cells. (F) T/NK cell marker expression. Dot plot showing expression of representative genes across T and NK cell subsets. (G) Myeloid cell heterogeneity. UMAP map illustrating macrophage, monocyte, dendritic cell, and microglial subsets, color-coded by transcriptional identity. (H) Myeloid marker genes. Dot plot summarizing defining genes (SPP1, C1QC, FOLR2, APOE, CXCL10, MMP9) across macrophage and related phagocyte populations. (I) CD163 expression mapping. Feature plot showing the distribution and relative expression of CD163 across myeloid clusters to align transcriptomic and IMC phenotypes. (J) Spatial transcriptomics in breast cancer. RCTD-based deconvolution map illustrating spot-level composition in a representative primary breast cancer tissue section, highlighting CN1-like epithelial-immune regions. (K) Spatial transcriptomics in brain metastasis. RCTD deconvolution map showing cell-type composition in a representative brain metastasis section, highlighting CN9-like invasion-immunosuppression domains. BC, breast cancer; CN, cell neighborhood; IMC, imaging mass cytometry; NK, natural killer; RCTD, Robust Cell Type Decomposition; Tcm, central memory; Tem, effector/memory; Tex, exhausted T cell; Treg, regulatory T cell; UMAP, Uniform Manifold Approximation and Projection.

transcriptomics sections to estimate spot-level mixtures of epithelial, T/NK, and myeloid subsets alongside stromal and neural elements (figure 5J,K). The resulting compositional maps recapitulated CN1-like and CN9-like domains in situ. In representative BC tissue (figure 5J), spots enriched for epithelial (E-cadherin$^+$ programs) with memory T/B support and CD163$^-$CD11b$^-$/APOE$^+$ macrophages localized into compact CN1-like territories, mirroring the cohesive immune-permissive niches seen by IMC. In contrast, representative BrM sections (figure 5K) displayed CN9-like regions marked by increased proportions of invasive/stem-like epithelial states together with CD163$^+$ macrophage programs (eg, C1QC$^+$, SPP1$^+$) and exhausted T subsets (CD4$^+$ Tex/CD8$^+$ Tex, Treg), aligning with the IMC-defined invasion-immunosuppression domain.

Integrating single-cell and spatial transcriptomics validated the IMC-defined CN architecture and linked phenotypic states to transcriptional programs. CN1 corresponded to epithelial regions supported by APOE$^+$ macrophages, memory T/B cells, and antigen-presenting activity, reflecting an immune-permissive niche. In contrast, CN9 aligned with invasive and stem-like epithelial programs co-localized with CD163$^+$ macrophages and exhausted T cells, forming an invasion-immunosuppression domain. These integrated analyses reveal the molecular basis of CN-specific microenvironments driving the BC-to-BrM transition.

Mechanistic rewiring distinguishes immune-competent CN1 from adhesion-stress-suppressed CN9

Gene Set Enrichment Analysis (GSEA) delineated a sharp functional bifurcation between CN1 and CN9. CN1 was enriched for immune-competent programs, including T-cell receptor signaling, NK cell-mediated cytotoxicity, chemokine signaling, antigen processing and presentation, FcγR-mediated phagocytosis, leukocyte transendothelial migration, and Th1/Th2/Th17 differentiation (figure 6A). In contrast, CN9 upregulated adhesion and inflammation-stress pathways with immunosuppressive overtones, including cell adhesion molecules, NF-κB/NOD-like receptor and cytosolic DNA-sensing pathways, and PD-L1 expression/PD-1 checkpoint (figure 6B).

Single-Cell rEgulatory Network Inference and Clustering (SCENIC) regulon activity highlighted distinct control logics. CN9-associated regulons included SOX9, FOXM1, E2F2, FOSL1, PPARG, NR1H2 (LXR), SOX12, and TBX3—coherently mapping to invasion/stemness programs, cell-cycle drive, and lipid/metabolic rewiring. In CN1, regulons such as PRDM1, PAX5, MYB, STAT5A, NR3C1, and ARNTL were preferentially active, consistent with antigen-experienced lymphocyte differentiation, B/T-cell activation, and immune homeostasis. Together, the regulon atlas aligns with GSEA, with CN9 favoring myeloid tolerance, and CN1 sustaining adaptive immune competence (figure 6C).

In comparing BrM to BC within CN1, samples from BrM showed reduced activity in T-cell receptor and NK pathways, as well as decreased antigen-presenting cell chains and leukocyte migration. This indicates less effective antigen processing and effector cell development compared with BC. These findings support the expansion of CN9 and the collapse of CN1 during brain colonization (figure 6D). Similarly, when comparing BrM to BC within CN9, there was a notable decrease in antigen processing, presentation, and phagosome activity, which aligns with the tumor's immune evasion strategies involving myeloid cells in CN9, along with a relative downregulation of ribosome and proteasome programs. This suggests a low-translation, stress-adapted survival state in CN9 consistent with the observations in BrM (figure 6E).

Cell-state-resolved expression patterns revealed interaction patterns between cellular populations of interest (figure 6F). Coordinated upregulation of the CD47-SIRPA "don't-eat-me" axis across epithelial and myeloid compartments in CN9 indicate reinforced anti-phagocytic signaling (figure 6G,H). Growth arrest-specific 6 (GAS6)-AXL receptor tyrosine kinase (AXL)/MER proto-oncogene tyrosine kinase (MERTK) signaling was broadly detected across CD163$^+$ macrophage subsets (SPP1$^+$, C1QC$^+$, FOLR2$^+$, FCN1$^+$, CXCL10$^+$), consistent with enhanced efferocytosis, interleukin-10 (IL-10)/transforming growth factor beta (TGF-β) programs, apoptotic debris clearance, and durable tolerance (figure 6I). These axes jointly promote M2 orientation and reinforce the immunosuppressive ecology of CN9. Prostaglandin signaling was prominent in CN9, with elevated prostaglandin E synthase 2 and 3 (PTGES2/3) (PGE2 synthesis), prostaglandin E receptor 4 (PTGER4/EP4), nectin cell adhesion molecule (NECTIN) and T-cell immunoreceptor with Ig and ITIM domains (TIGIT) across epithelial, myeloid, and T-cell states, supporting widespread suppression and Treg stabilization (figure 6J,K). Cross-compartment ligand-receptor mapping outlined a cohesive network sustaining CN9 structure and function. Tumor-macrophage interactions were dominated by GAS6-AXL/MERTK (tolerance/M2 polarization) and CD47-SIRPA (anti-phagocytosis), that support epithelial persistence and myeloid residency. Tumor/myeloid T-cell edges featured NECTIN2-TIGIT (exhaustion) and PGE2-EP4 (Treg support and effector dampening; online supplemental figure S3B).

Together, pathway, regulon, and ligand-receptor evidence converge on a model in which CN9 evolves into a perivascular, adhesive, immunosuppressive niche that facilitates metastatic seeding and long-term persistence, while CN1—the local immune gateway—collapses, disabling clearance and surveillance. This mechanistic synthesis explains the spatial ecology shift from BC to BrM: a CN1-to-CN9 transition driven by extracellular matrix/integrin adhesion, GAS6-Tyro3, Axl, and Mer receptor tyrosine kinase family (TAM) tolerance (M1 to M2), CD47-mediated anti-phagocytosis, and NECTIN2-TIGIT/PGE2-EP4 T-cell suppression, collectively stabilizing CN9 and conferring metastatic competence (figure 6L).

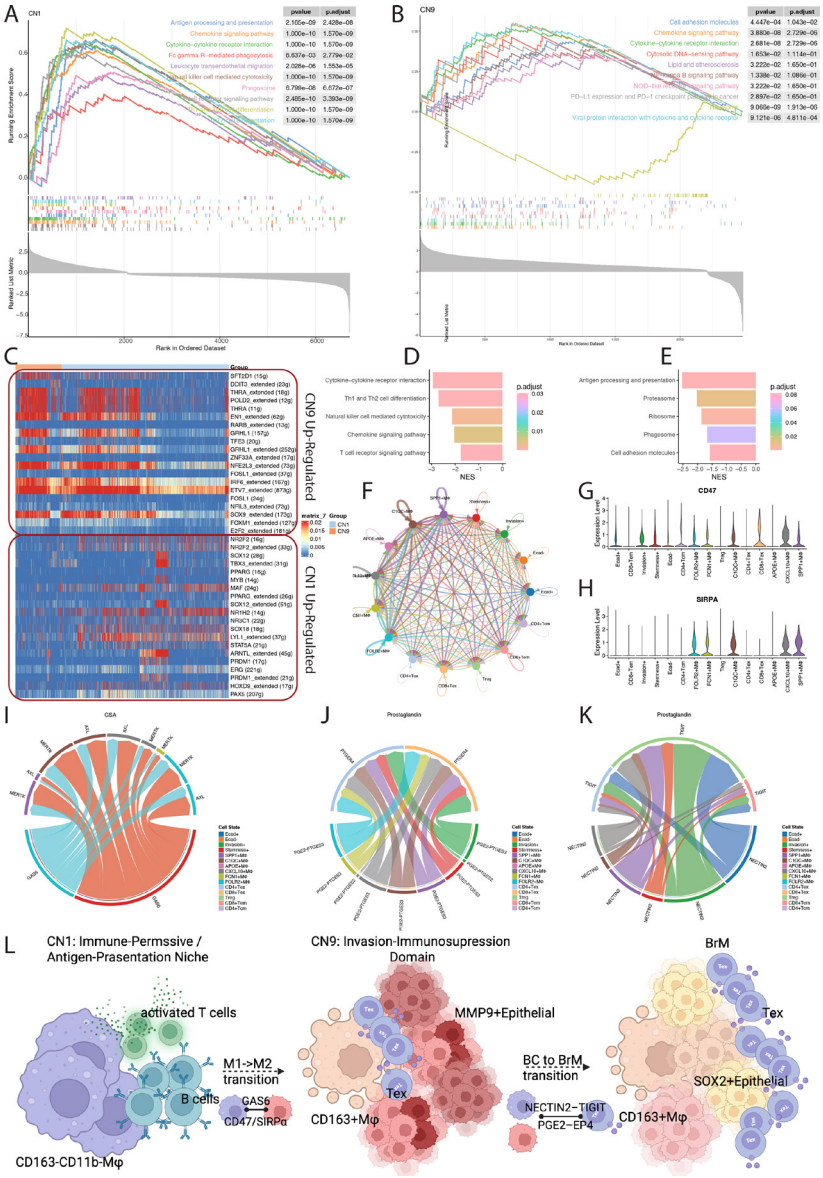

Figure 6 Integrated pathway, regulon, and ligand-receptor analyses define the mechanistic divergence between CN1 and CN9. (A) Immune-enriched pathways characterize CN1 functional programs. GSEA plots showing immune activation and antigen-presentation pathways enriched in CN1. The table to the right lists corresponding p values and adjusted p values for representative gene sets. (B) Adhesion-associated and checkpoint-associated pathways dominate CN9 signaling. GSEA plots depicting enrichment of cell adhesion, NF-κB/NOD-like receptor, and PD-1/PD-L1 checkpoint pathways in CN9, with significance scores summarized in the right panel. (C) Distinct transcriptional regulon landscapes define CN1 and CN9. SCENIC heatmap displaying activity of transcription factor regulons, with CN9-enriched modules (eg, SOX9, FOXM1, E2F2) and CN1-enriched modules (eg, PRDM1, PAX5, STAT5A) indicated. (D–E) Site-specific pathway modulation within CN1 and CN9 across BC and BrM. Bar plots showing NES of representative pathways when comparing BrM to BC samples within CN1 (D) and CN9 (E); the color gradient indicates adjusted p values. (F) Multicellular interaction network across major cell states. Network visualization summarizing predicted ligand-receptor interactions between epithelial, macrophage, and T-cell populations derived from integrated spatial and single-cell data. (G–H) Expression profiles of anti-phagocytic checkpoints CD47 and SIRPA. Violin plots showing single-cell expression distributions of CD47 (G) and SIRPA (H) across epithelial and macrophage subsets involved in CN9 immune suppression. (I–K) Chord diagrams illustrating key ligand-receptor signaling axes. Circular plots representing intercellular interactions for (I) GAS6-AXL/MERTK signaling, (J) PGE2-PTGER (EP4) signaling, and (K) NECTIN2-TIGIT immune checkpoint pathways, with ribbon width proportional to interaction strength. (L) Conceptual model summarizing spatial-functional transition from CN1 to CN9. Schematic illustration depicting CN1 as an immune-permissive, antigen-presentation niche and CN9 as an invasion-dominated and immunosuppression-dominated domain expanded in brain metastases. AXL, AXL receptor tyrosine kinase; BC, breast cancer; BrM, brain metastases; CN, cell neighborhood; EP4, prostaglandin E2 receptor 4; GAS6, growth arrest-specific 6; GSEA, Gene Set Enrichment Analysis; MERTK, MER proto-oncogene tyrosine kinase; MMP, matrix metalloproteinase; NES, normalized enrichment scores; PD-1, programmed cell death protein 1; PD-L1, programmed death-ligand 1; PGE2, prostaglandin E2; PTGER, prostaglandin E receptor; SCENIC, Single-Cell rEgulatory Network Inference and Clustering; Tex, exhausted T cell; TIGIT, T-cell immunoreceptor with Ig and ITIM domains.

Mechanistic analyses revealed that CN9 adopts an adhesion-driven, stress-adapted, and immunosuppressive state, while CN1 maintains immune competence. In BrM, CN9 expands and strengthens GAS6-TAM, CD47-SIRPA, and NECTIN2-TIGIT/PGE2-EP4 signaling, promoting macrophage tolerance and T-cell exhaustion, whereas CN1 loses antigen presentation and effector programs. Together, these findings define a CN1-to-CN9 transition that dismantles local immune surveillance and establishes a stable, metastasis-supportive niche in brain lesions.

Combined AXL inhibition and CD47 blockade suppress brain metastatic growth and remodel the macrophage microenvironment

A 4T1-Luc BC brain metastasis model was generated by carotid artery injection, followed by treatment with phosphate-buffered saline (PBS), R428, anti-CD47 antibody, or the combination regimen (figure 7A). Tumor progression was monitored longitudinally by bioluminescence imaging on D1, D3, D6, and D9. As shown in figure 7B,C, the PBS group exhibited a progressive increase in bioluminescence signal over time, consistent with continued tumor growth in the brain. In contrast, both R428 and anti-CD47 monotherapy reduced signal intensity to a certain extent compared with the control group. The combination group showed the lowest bioluminescence signal during follow-up, indicating a stronger inhibitory effect on brain metastatic progression. Notably, although the overall distribution of bioluminescence signals appeared broadly similar across groups at D9, the combination group displayed markedly weaker signal intensity, suggesting reduced tumor burden within established metastatic regions. Quantitative analysis confirmed that bioluminescence intensity in the combination group was significantly reduced compared with the PBS group (p=0.016). In addition, the combination group also showed significantly lower signal intensity than the R428 and anti-CD47 monotherapy groups (p=0.008 and p=0.004, respectively) (figure 7C).

These imaging findings were further supported by histopathological examination. H&E staining revealed extensive metastatic lesions with dense tumor cell infiltration in the PBS group. By comparison, the R428 and anti-CD47 groups displayed smaller metastatic foci. In the combination group, tumor areas were further reduced, accompanied by more prominent stromal and immune cell infiltration within the lesion regions (figure 7D).

Changes in the tumor microenvironment were further assessed by mIHC staining of brain metastatic lesions. Pan-CK and SOX2 signals were decreased in the treatment groups relative to PBS, with the most marked reduction observed in the combination group, supporting a decrease in tumor burden and stemness-associated tumor features. Meanwhile, CD68 staining showed increased macrophage infiltration after treatment, particularly in the combination group. In contrast, CD163 did not increase in parallel with CD68 and instead showed a relative decrease across treatment groups, especially in the combination group, suggesting that treatment altered macrophage composition rather than simply increasing the abundance of immunosuppressive macrophages (figure 7E).

To further characterize the molecular consequences of combination therapy, we performed cerebrospinal fluid (CSF) proteomic profiling using the NuLISA 120-plex Mouse Inflammation Panel (n=2 per group). Gene Set Variation Analysis (GSVA) revealed a striking divergence between treatment groups. Among the selected immune activation pathways—IL-1 signaling, tumor necrosis factor/nuclear factor kappa B (NF-κB), toll-like receptor, nucleotide-binding oligomerization domain (NOD)-like receptor, cytosolic DNA sensing, T-cell costimulation, IL-12, and interferon-γ response—the combination group showed the highest enrichment scores and the PBS group the lowest. Notably, T-cell costimulation (GSVA score: Combo=0.72 vs PBS=−0.26) and IL-1 signaling (Combo=0.66 vs PBS=−0.48) showed the strongest treatment effects, indicating robust activation of both innate and adaptive antitumor immunity in the CSF compartment. Conversely, two protumoral pathways—VEGF signaling and growth factor-receptor tyrosine kinase–phosphoinositide 3-kinase (RTK-PI3K) signaling—were highest in PBS and lowest in the combination group, with single-agent groups showing intermediate effects in both directions (figure 7F).

Overall, combined AXL inhibition and CD47 blockade produced the strongest suppression of brain metastatic growth in this model and was accompanied by enhanced immune infiltration and a shift in the macrophage landscape within metastatic lesions.

DISCUSSION

Although major progress has been made in charting the systemic immune landscape of metastatic BC, the spatial and functional organization of the brain metastatic niche remains poorly defined.[13 26–28] Most previous studies relied on bulk transcriptomics or limited immunohistochemistry, methods that cannot resolve fine cellular neighborhoods or the direct cell–cell interactions that sustain metastatic growth.[29] Recent single-cell analyses have delineated the immune and stromal diversity of BC and its BrM. For instance, Xie *et al* constructed a single-cell atlas of BC BrM and identified interleukin enhancer-binding factor 2 (ILF2) as a potential therapeutic target,[30] while Klughammer *et al* integrated single-cell and spatial transcriptomic data to uncover molecular programs underlying metastatic adaptation.[28] Nevertheless, these studies rarely addressed how distinct cell populations are spatially organized or how they interact within the metastatic microenvironment. To fill this gap, we applied high-plex IMC integrated with public scRNA-seq and ST data to construct a multidimensional map of primary breast tumors and BrM, enabling direct comparison of cellular composition, intercellular communication, and ligand-receptor signaling.

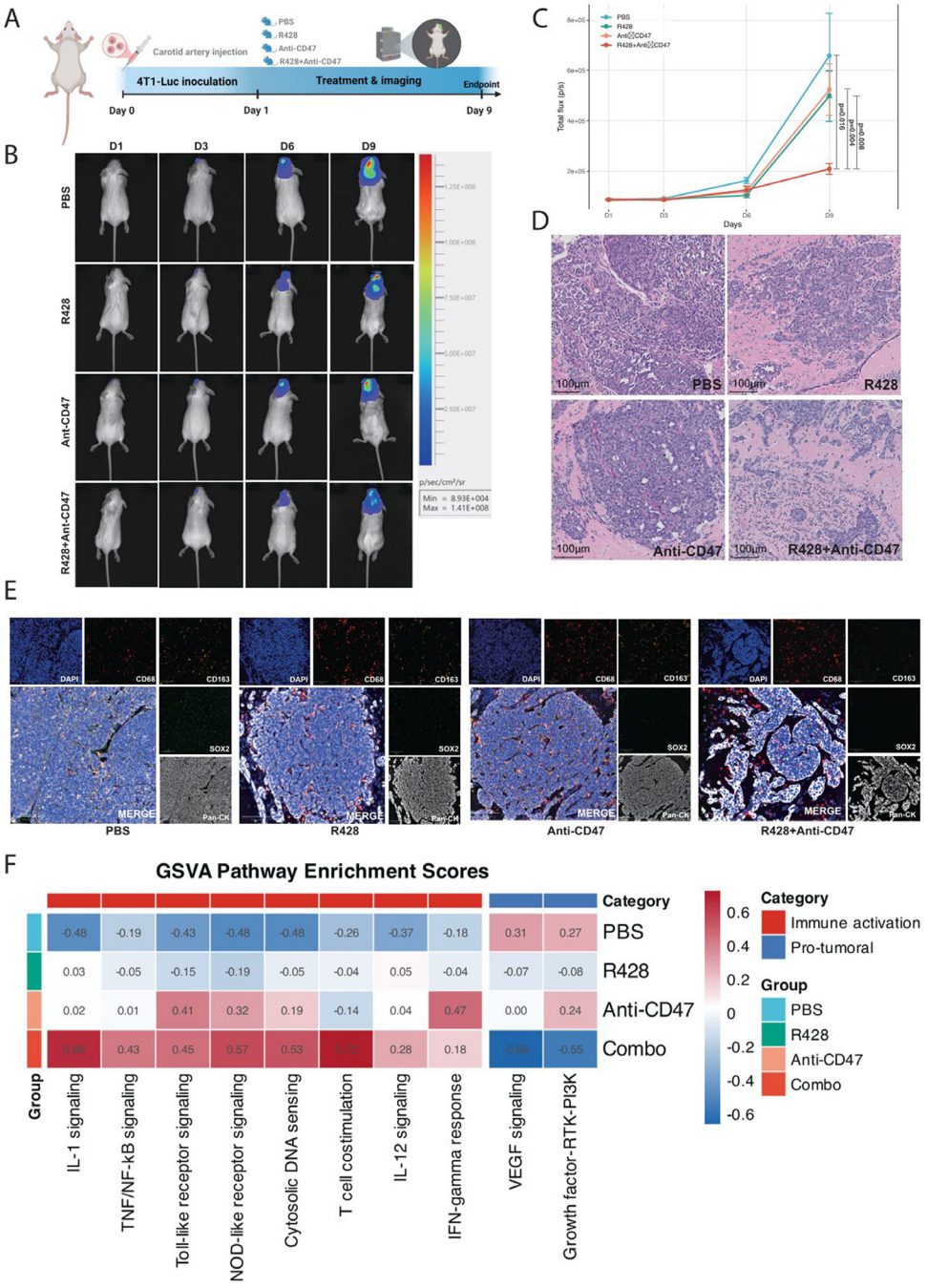

Figure 7 In vivo evaluation of therapeutic efficacy in a breast cancer brain metastasis model. (A) Schematic overview of the in vivo experimental design. (B) Representative bioluminescence imaging of tumor progression in mice from each treatment group at D1, D3, D6, and D9 after tumor cell inoculation. Signal intensity reflects tumor burden in the brain. (C) Quantification of bioluminescence signals in the PBS, R428, anti-CD47, and R428+anti-CD47 groups at D1, D3, D6, and D9 after tumor cell inoculation. Total photon flux is shown as photons per second, with data presented as mean±SEM. Blue, PBS group; green, R428 group; orange, anti-CD47 group; red, R428+anti-CD47 group. P values indicate comparisons between the combination group and the indicated treatment groups at D9. (D) H&E staining of brain sections showing metastatic tumor lesions in each group. Representative images illustrate differences in tumor burden and tissue architecture (scale bar, 100 μm). (E) Multiplex immunohistochemistry staining of brain metastatic lesions. Nuclei are labeled with DAPI (blue), macrophages with CD68 (red), $CD163^{+}$ macrophages with CD163 (orange), tumor stemness-associated marker SOX2 (green), and epithelial tumor cells with Pan-CK (white). Representative images demonstrate the spatial distribution of tumor cells and macrophage populations across treatment groups (scale bar, 100 μm). (F) GSVA pathway enrichment heatmap of CSF proteomic profiling. NuLISA 120-plex Mouse Inflammation Panel was used to profile CSF from all treatment groups (n=2 per group). Heatmap displays group-mean GSVA enrichment scores for immune activation pathways (left) and protumoral pathways (right). CSF, cerebrospinal fluid; DAPI, 4′,6-diamidino-2-phenylindole; GSVA, Gene Set Variation Analysis; IFN, interferon; IL, interleukin; NF-κB, nuclear factor kappa B; NOD, nucleotide-binding oligomerization domain; PBS, phosphate-buffered saline; RTK-PI3K, receptor tyrosine kinase-phosphoinositide 3-kinase; TNF, tumor necrosis factor; VEGF, vascular endothelial growth factor.

Our data reveal a progressive re-engineering of the metastatic immune ecosystem. IMC defined nine major cell classes and demonstrated marked shifts in composition between primary and metastatic sites. Primary tumors contained abundant epithelial cells and balanced immune and stromal compartments, whereas BrM showed a reduced epithelial fraction and enrichment of stromal and myeloid elements. High-resolution subclustering uncovered a spectrum of functional states within epithelial, myeloid, and T-cell lineages—including proliferating, invasion-like, and stem-like epithelial cells; multiple macrophage phenotypes; and distinct memory, regulatory, effector, and exhausted T cells. These findings complement and extend prior single-cell atlases by revealing how specific phenotypes are reorganized and how they interact spatially and molecularly within the metastatic brain.

Among the most striking features was the dynamic remodeling of macrophage populations defined by CD163 expression. This observation aligns with recent single-cell work: for instance, Cheng *et al* constructed a pan-cancer atlas of infiltrating myeloid cells and demonstrated divergent transcriptional programs among macrophage subsets[31]; Zhang *et al* profiled tumor-associated macrophages in BC and linked CD163-associated subsets to immunosuppressive signaling[32]; and Chen *et al* showed that tumor-derived microenvironmental cues modulate macrophage polarization dynamics via metabolic and ionic pathways.[33] Together, these studies support the context-dependent role of $CD163^+$ versus $CD163^-CD11b^-$ macrophages and strengthen the rationale for investigating their remodeling during metastatic progression.

In BrM, $CD163^-CD11b^-$ macrophages were significantly reduced, whereas $CD163^+$ macrophages did not show a statistically significant change compared with primary tumors. This suggests that macrophage remodeling in BrM may be associated with depletion of immune-supportive $CD163^-$ subsets, whereas $CD163^+$ macrophages do not show a significant quantitative change. This shift was accompanied by an expansion of $PD\text{-}L1^+$ and $S100A9^+$ myeloid subsets, suggesting that the metastatic niche promotes alternative immunosuppressive programs and remodels macrophage-T cell interactions rather than simply amplifying classical M2 states. Similar macrophage reprogramming has been reported in melanoma and lung cancer BrM, where Klemm *et al*[34] and Zhang *et al*[35] described a convergent shift of tumor-associated macrophages toward $SPP1^+$ and $C1QC^+$ immunoregulatory states with reduced antigen-presenting potential. These findings support the notion that macrophage functional reprogramming—rather than lineage expansion of specific subsets such as $CD163^+$ cells—represents a common adaptive strategy of brain-colonizing tumors.

Consistent with this paradigm, our findings suggest that $CD163^+$ macrophages, despite lacking significant changes in overall abundance, are preferentially enriched within the expanded immunosuppressive CN9 niche in BrM. This highlights that their functional impact is dictated by spatial organization rather than quantitative variation, underscoring the importance of niche-level immune regulation in metastatic progression. Spatial neighborhood analysis underscored this progressive transition. Immune-permissive regions enriched for memory T cells, B cells, and $CD163^-CD11b^-$ macrophages (CN1) were prominent in primary tumors but contracted markedly in brain lesions. Conversely, an immunosuppressive neighborhood (CN9) containing $MMP9^+$ epithelial cells, exhausted T cells, $PD\text{-}L1^+$ and $S100A9^+$ myeloid cells, and $CD163^+$ macrophages expanded within the metastatic brain. Ligand-receptor inference revealed extensive cell–cell communication within CN9, dominated by PD-1/PD-L1, GAS6-TAM, NECTIN2-TIGIT, and PGE2-EP4 pathways, which collectively reinforce local immune suppression and tissue adaptation. The concurrent preservation of $CD163^+$ macrophages within this expanded niche and enrichment of these inhibitory circuits suggest a coordinated transition from an antigen-presenting, immune-supportive niche to a structurally organized, immunosuppressive one. Similar suppressive signaling networks have been described in glioblastoma and leptomeningeal metastases, supporting the broader relevance of our observations to the CNS metastatic immune ecosystem.[34] Importantly, the expansion of CN9 together with the preserved presence of $CD163^+$ macrophages suggests that these cells act as integral components of the immunosuppressive niche, functioning within a coordinated cellular network rather than as independently expanded populations.

Targeting macrophage-centered immunoregulatory pathways provides a rational strategy to interrogate the functional relevance of the CN9 niche identified in our spatial analyses. The AXL receptor, a central component of the GAS6–TAM signaling axis, has been implicated in promoting immunosuppressive macrophage polarization, efferocytosis, and tumor cell survival, thereby contributing to immune evasion within the tumor microenvironment.[36] In parallel, CD47 functions as a dominant "don't-eat-me" signal that inhibits macrophage-mediated phagocytosis through engagement of SIRPα. Blockade of CD47 has been shown to enhance macrophage phagocytic activity and facilitate antigen presentation,[37] but its efficacy is often limited by the persistence of immunosuppressive macrophage states.

In this context, combined inhibition of AXL signaling and CD47-mediated anti-phagocytic signaling represents a complementary strategy that simultaneously disrupts immunosuppressive macrophage programming and restores macrophage effector function. Our in vivo findings support this concept, showing that such dual targeting is associated with reduced metastatic burden and increased immune infiltration. Notably, the dissociation between increased $CD68^+$ macrophage infiltration and the lack of expansion in $CD163^+$ subsets suggests that therapeutic efficacy is not driven by expansion of specific macrophage populations, but rather by reconfiguration of macrophage functional states within the metastatic niche.

Importantly, these observations reinforce the notion that CD163$^+$ macrophages, as integral components of the expanded CN9 niche, contribute to immune regulation through their spatial positioning and interaction networks rather than changes in their absolute abundance. Interestingly, in the context of therapeutic intervention, a relative decrease in CD163$^+$ macrophages was observed alongside reduced tumor burden and enhanced immune infiltration, suggesting that CD163$^+$ macrophages may participate in the reshaping of the tumor microenvironment under treatment. While this does not exclude a potential contribution of their abundance, it further supports the idea that the functional role of CD163$^+$ macrophages is context-dependent and closely linked to niche-specific organization. Together, these findings highlight that effective immunomodulation in BrM may require coordinated targeting of macrophage-associated signaling pathways and spatial niche architecture, rather than focusing solely on the expansion or depletion of individual macrophage subsets.

These findings have clear clinical implications. The contraction of CN1 and expansion of CN9 likely disrupt antigen presentation and diminish productive macrophage–T cell interactions, helping to explain the limited efficacy of PD-1/PD-L1 inhibitors in BC BrM. Notably, imaging and molecular profiling studies have demonstrated that CD163$^+$ tumor-associated macrophages play critical roles in modulating immune infiltration and therapy response. For example, intravital and nanobody-based imaging of CD163$^+$ tumor-associated macrophages has revealed their spatial redistribution during tumor progression and treatment, suggesting that depletion of this subset may compromise antigen presentation and T-cell priming.[38] Moreover, preclinical data show that PD-1/PD-L1 blockade efficacy in BrM is strongly constrained by myeloid-cell-driven immune exclusion and defective antigen presentation.[39] At the same time, the expansion of CN9 and the enrichment of inhibitory ligand-receptor circuits reinforce local tolerance. Therapeutic strategies that target these intercellular signaling pathways—such as blockade of TAM receptors (AXL/MERTK), TIGIT, or prostaglandin-EP4 signaling—or interventions designed to preserve or reconstitute CD163$^+$ macrophage–T-cell communication may help restore antitumor immunity in the metastatic brain. For instance, inhibition of the MerTK receptor has been shown to reduce immunosuppressive macrophage behavior and enhance antigen presentation in glioma and lung cancer models.[40] Co-inhibition of TIGIT and PD-1/PD-L1 checkpoints improved survival and restored CD8$^+$ T-cell effector function in preclinical intracranial tumor models.[41] These findings support a model in which targeting niche-level immunosuppressive circuits, rather than individual macrophage subsets alone, may be required to restore antitumor immunity in BrM.

We acknowledge several limitations. Although our cohort is larger than in most prior IMC studies, the number of regions of interest is still modest and may not capture the full interpatient heterogeneity of BC BrM. Our antibody panel, while extensive, cannot encompass every relevant signaling pathway, and functional validation of predicted cell–cell interactions was further supported by the in vivo combination therapy experiment described above. As all patients in the current cohort were treatment-naïve at the time of tissue collection, future studies should incorporate post-therapy specimens and longitudinal samples to determine when during metastatic evolution the loss of CD163$^-$ macrophages and the emergence of CD163$^+$/PD-L1$^+$ states occur. Furthermore, our in vivo validation used a single syngeneic model (4T1-Luc) with treatment initiated on day 1 after intracarotid inoculation. As established in pilot studies, the rapid progression of this model to humane endpoints precluded delayed-treatment paradigms; our findings therefore address the peri-colonization stage of brain metastasis rather than established macroscopic lesions. Extension to delayed-treatment designs, orthotopic models, and spontaneous metastasis systems will be needed to confirm therapeutic relevance in clinically established disease. The CSF proteomic profiling (NuLISA 120-plex Mouse Inflammation Panel) was conducted as an exploratory pilot with n=2 per group, and larger-cohort validation will be needed to establish statistical robustness and to rule out interanimal variability.

In conclusion, our integrative spatial analysis delineates a stepwise ecological transition as BC colonizes the brain. Using high-plex imaging mass cytometry combined with single-cell and spatial transcriptomics, we uncovered a progressive loss of immune-permissive neighborhoods and a concomitant expansion of an immunosuppressive, invasion-oriented niche. This shift is accompanied by a dynamic reprogramming of macrophage populations, in which CD163$^+$ macrophages remain present but become embedded within an expanded immunosuppressive CN9 niche, and by profound alterations in T-cell states. Within CN9, we identified enriched intercellular signaling axes—including PD-1/PD-L1, GAS6–TAM, NECTIN2–TIGIT, and PGE2–EP4—that collectively reinforce immune evasion and metastatic growth. Together, these findings provide a spatially resolved mechanistic framework for understanding why BC BrM respond poorly to immune checkpoint blockade and highlight actionable therapeutic targets aimed at restoring antigen presentation, re-establishing CD163$^+$ macrophage–T-cell crosstalk, and dismantling the suppressive ligand-receptor networks that dominate the metastatic niche.

Our integrated spatial multi-omics analysis reveals a shift from an immune-active niche to an invasion-immunosuppressive domain during BC brain metastasis. The preservation of CD163$^+$ macrophages within the expanded CN9 niche and activation of GAS6–TAM, NECTIN2–TIGIT, PGE2–EP4, and CD47–SIRPα signaling collectively drive immune evasion and metastatic persistence. These findings provide mechanistic insight into the failure of immune surveillance in brain lesions and highlight potential therapeutic targets to restore antitumor immunity.

MATERIALS AND METHODS

Patient samples and ethical approval

Human primary BC and matched BrM were collected from Guangdong Provincial People's Hospital with approval from the institutional ethics committee. All patients were treatment-naïve at the time of tissue collection. The cohort comprised 8 female patients (3 TNBC, 3 HER2-positive, and 2 LB), contributing 20 BC ROIs from 5 patients and 40 BrM ROIs from 8 patients (4–12 ROIs per patient, median 8; see online supplemental table S2). No randomization or blinding was applied. All available cases meeting inclusion criteria were analyzed. Patient age, sex, and clinicopathological features are summarized in online supplemental table S1. All ROIs were acquired at a uniform fixed size of 500 µm × 500 µm (0.25 mm^2) at 1 µm resolution on the Hyperion Imaging System. ROIs were selected by an experienced pathologist on H&E-stained serial sections, targeting histologically confirmed tumor regions containing both malignant cells and adjacent stromal/immune compartments, while avoiding large necrotic areas, folding artifacts, or tissue damage (online supplemental table S2).

Imaging mass cytometry

Consecutive 4 µm formalin-fixed paraffin-embedded sections were deparaffinized, rehydrated, and subjected to Tris-EDTA antigen retrieval (pH 9.0, 95°C, 20 min). A 39-plex metal-conjugated antibody panel (online supplemental table S3) was used to profile tissue structures, myeloid, lymphoid, and functional-related compartments, including Pan-cytokeratin, CK7, CK8, E-cadherin, P2Y12, GFAP, Olig2, NeuN, Collagenl, αSMA, Vimentin, CD31, CD45, CD45RO, CD16, CD14, CD11b, CD163, CD68, CD11c, CD3, CD4, CD8, FoxP3, CCR7, CD20, CD57, S100A9, FAP, cleaved caspase-3, PDPN, IDO-1, PD-L1, PD-1, granzyme B, Ki-67, HLA-DR, SOX2, and MMP9. Carrier-free primary antibodies were metal-labeled with the Maxpar X8 kit (Standard BioTools) and validated on control tissues. After overnight incubation at 4°C with the antibody cocktail, slides were counterstained with iridium intercalator and imaged on a Hyperion Imaging System (Standard BioTools) at 1 µm resolution with identical acquisition parameters for all specimens.[42]

Image processing and single-cell segmentation

Raw mass cytometry data (MCD) files were converted to multi-channel images in Tagged Image File Format (TIFF) and normalized for channel drift. Pixel classification was performed in Ilastik to generate nuclear, cytoplasmic/membrane, and background probability maps. CellProfiler pipelines then applied watershed segmentation seeded by nuclear masks to delineate individual cells. Per-cell marker intensities were calculated as median values, spillover-corrected, and arcsinh-transformed with a cofactor of 5. Objects with a segmented area outside 20–800 $µm^2$ were excluded as likely segmentation artifacts (subcellular fragments or under-segmented clusters).[43]

Cell phenotype annotation and dimensionality reduction

Downstream analyses were conducted in R using Seurat and Cytofkit2. Phenograph clustering (k=10) identified cell populations which were visualized with UMAP. Annotation relied on canonical marker combinations, for example, Pan-cytokeratin$^+$ E-cadherin$^+$ for epithelial cells, CD31$^+$ for endothelial cells, CD45$^+$ CD3$^+$ for T lymphocytes, and CD45$^+$ CD68$^+$ CD163$^+$ for monocyte-macrophage lineages. Functionally distinct subsets were defined by Ki-67$^+$ (proliferating), cleaved caspase-3$^+$ (apoptotic), SOX2$^+$ (stemness-like), MMP9$^+$ (invasive), S100A9$^+$ and PD-L1$^+$, HLA-DR$^+$. This hierarchical annotation strategy was informed by recent multiplexed spatial proteomic studies employing the same logic.[17 18]

Spatial neighborhood analysis

Spatial CNs were constructed with imcRtools by identifying the 10 nearest neighbors for every cell. Cells were assigned to reproducible communities (CN1–CN10, each assigned a descriptive name based on its dominant compositional features; see Results) across all images. Neighborhood enrichment was quantified as log2 (observed/expected) ratios, and statistical significance was assessed by permutation testing. Distances of specific cell populations, including SOX2+ or MMP9+epithelial cells, PD-L1+macrophages, and Tregs, to CN borders were calculated to evaluate their preferential localization at invasive fronts.

Ligand-receptor and pathway analyses

Ligand-receptor interactions were inferred from the integrated scRNA-seq data using CellChat (see cell–cell communication analysis below for full parameters). GSEA was conducted with clusterProfiler against Kyoto Encyclopedia of Genes and Genomes (KEGG) and Hallmark gene sets, focusing on chemokine signaling, T-cell receptor signaling, antigen processing and Th-cell differentiation.

Public single-cell RNA-sequencing integration

Public scRNA-seq datasets from GEO (accession number: GSE225600, GSE186344 and HRA006468) were processed in R using Seurat (V.4.0.1): low-quality cells were removed based on gene and unique molecular identifier (UMI) counts and mitochondrial content, doublets were excluded, data were normalized and log-transformed, highly variable genes were selected, principal component analysis was performed, batch effects were corrected when necessary, a shared nearest-neighbor graph was constructed for Leiden clustering, and UMAP was used for visualization; lineage-specific subsets (epithelial, T/NK, myeloid) were re-clustered with the same workflow, program scores were calculated with AddModuleScore as needed, and dot plots were generated with Seurat to display average expression and the proportion of expressing cells across clusters.[44 45]

Spatial transcriptomics

Spatial gene-expression data were obtained from Zenodo (https://zenodo.org/records/14247036) and

GEO database (accession number: GSE179572). Raw sequencing reads were aligned to the GRCh38 reference genome and quantified to generate spot-level count matrices using Space Ranger (10x Genomics). Spots with low UMI counts, low gene counts, or high mitochondrial transcript percentage were removed after quality-control filtering. The filtered count matrix was normalized and log-transformed, and highly variable genes were identified. Dimensionality reduction was performed with principal component analysis, and spatial clustering and visualization were carried out using Seurat V.4.0.1.[46]

Multimodal data integration strategy

IMC, scRNA-seq, and spatial transcriptomics were not fused into a single data matrix; instead, each modality was analyzed with established tools and the results were integrated at the interpretive level through shared cell-type annotations. Cellular neighborhoods were first defined from IMC data by computing, for each cell, the cell-type composition of its 10 nearest spatial neighbors and clustering the resulting composition vectors by k-means.[47] Public scRNA-seq datasets were integrated with Seurat using reciprocal principal component analysis (PCA). Major lineages (epithelial, T/NK, myeloid) were re-extracted and re-clustered independently to resolve fine subclusters. Transcriptional subclusters were aligned to IMC phenotypes via shared canonical markers (eg, CD163 for macrophages, PDCD1/CTLA-4 for exhausted T cells). To map IMC-defined spatial archetypes onto Visium spatial transcriptomics data, RCTD deconvolution was applied to each Visium spot using the matched scRNA-seq dataset as reference,[48] yielding per-spot cell-type proportion estimates. Spots were assigned to a CN when their deconvolved composition satisfied the corresponding cell-type co-occurrence rule: CN9-like spots required co-presence of stemness/invasion-associated epithelial cells, CD163$^+$ macrophage subtypes (SPP1$^+$, C1QC$^+$, CXCL10$^+$, FCN1$^+$, or FOLR2$^+$), and exhausted/regulatory T cells; CN1-like spots required APOE$^+$ macrophages and memory T or B cells. Ligand-receptor analysis was performed on the scRNA-seq compartment using CellChat,[49] subsetting to cell types enriched in each CN of interest.

Cell–cell communication analysis

Cell–cell communication was inferred from the normalized single-cell expression matrix using CellChat with the human ligand-receptor database. Overexpressed ligands/receptors were identified per cluster, probability of signaling between sender-receiver pairs was estimated under the built-in permutation framework, and pathway-level information flow was computed.[50] Interaction networks and chord diagrams were generated with default visualization functions after false discovery rate correction. For CN-specific analyses, the scRNA-seq object was subset to cell types enriched in each CN of interest (eg, CN9: CD163$^+$ macrophage subtypes, exhausted T cells, Treg, and invasion-associated epithelial cells) before running CellChat to infer niche-restricted signaling.

Pathway enrichment

Pathway activity per cluster (or condition) was assessed by gene set enrichment using clusterProfiler with KEGG and Hallmark collections. Ranked gene lists were derived from model-based or non-parametric differential testing, and adjusted p values were reported using the Benjamini-Hochberg procedure.

Transcription factor activity scoring

Transcription factor regulon activity was inferred using SCENIC.[51] Briefly, co-expression modules were identified from the normalized single-cell expression matrix using GRNBoost2, and cis-regulatory motif enrichment was assessed with RcisTarget to retain only modules supported by proximal transcription factor binding motifs. The resulting regulons were visualized as heatmaps for comparative assessment across cell states and spatial niches.

In vivo tumor models

All animal procedures were conducted in accordance with institutional guidelines, approved by the Institutional Animal Care and Use Committee (IACUC) of Shenzhen Lingfu Tuopu Biotechnology (Approval No. TOP-1PZ-GM260205), and performed in compliance with internationally accepted principles for the care and use of laboratory animals. Female BALB/c mice (8 weeks old) were used in all experiments, with five mice included in each group. The experimental unit was one individual mouse. No predefined inclusion or exclusion criteria were applied during the animal experiments or data analysis. Mice were randomly allocated to the experimental groups. Mice were maintained under specific pathogen-free conditions with controlled temperature and humidity, a 12 hours light/dark cycle, and free access to sterilized food and water.

An experimental BC brain metastasis model was established using luciferase-labeled 4T1 cells (4T1-Luc). Briefly, 2×10^5 cells suspended in 50 µL PBS were injected via the carotid artery to induce brain metastatic colonization. Therapeutic intervention was initiated on the day after tumor cell inoculation (D1). This early-treatment schedule was informed by pilot studies demonstrating that the aggressive progression of the 4T1-Luc intracarotid model (rapid neurological deterioration within 9–10 days) restricted the available treatment window to pre-colonization and early colonization stages while remaining within the IACUC-approved humane endpoints. Mice in the control group received vehicle treatment. Mice in the R428 monotherapy group were administered R428 (Bemcentinib, MedChemExpress, HY-15150) at 50 mg/kg by oral gavage once daily. Mice in the anti-CD47 monotherapy group received anti-CD47 antibody (MIAP301, MedChemExpress, HY-P990131) by intraperitoneal injection at 100 µg per mouse two times

per week. Mice in the combination treatment group received both R428 (50 mg/kg, oral gavage, daily) and anti-CD47 antibody (100 µg per mouse, intraperitoneal injection, two times per week). Tumor progression was monitored by in vivo bioluminescence imaging on D1, D3, D6, and D9. Mice were euthanized on D9, and brain tissues were collected for subsequent histological and immunofluorescence analyses.

Histological analysis

Brain tissues were fixed in 10% neutral-buffered formalin, embedded in paraffin, and sectioned at 4–5 µm thickness. H&E staining was performed according to standard histopathological procedures. Stained sections were used to evaluate tumor burden, tissue architecture, and treatment-related morphological changes. Whole-slide brightfield images were acquired using a Mantra Quantitative Pathology Workstation (Akoya).

Multiplex immunohistochemistry

mIHC staining was performed on paraffin-embedded brain sections to characterize tumor and immune components within metastatic lesions. Sections were stained with antibodies against CD68 (HUABIO, HA722285), CD163 (Abcam, ab182422), SOX2 (ABclonal, A0561), and Pan-CK (Abcam, ab308262), with DAPI used for nuclear counterstaining. Multispectral images were acquired using the Mantra imaging platform (Akoya), and representative regions were analyzed to assess the spatial distribution of tumor cells and macrophage populations.

NuLISA analysis

CSF was collected from mice in all four treatment groups (n=2 per group) at endpoint (D9) and profiled using the NuLISA 120-plex Mouse Inflammation Panel. Normalized protein quantification (NPQ) values were computed for each target. GSVA was applied to the NPQ expression matrix using curated gene sets from MSigDB (KEGG Legacy, KEGG Medicus, Hallmark, and Reactome collections; gene sets with ≥3 overlapping NuLISA targets were retained). Pathway-level enrichment scores were computed per sample and averaged within each treatment group. This initial profiling was performed with a limited sample size (n=2 per group) and should be regarded as an exploratory pilot analysis; the pathway-level results reported here indicate directional trends rather than formal statistical differences.

Statistical analysis

All statistical tests were two-sided. All compositional analyses were performed on cell-type and CN proportions (fraction of each type relative to total segmented cells per ROI), which inherently normalize for variation in total cell yield. Given the uniform 0.25 mm^2 ROI area, proportion-based analysis is equivalent to density-based comparison (cells/mm^2) up to a constant scaling factor. Differences between primary and metastatic tumors were assessed with Wilcoxon rank-sum or Kruskal-Wallis tests, followed by Benjamini-Hochberg correction. Correlations were evaluated using Spearman's rank test. P value<0.05 was considered significant. Analyses were repeated with varying clustering parameters to confirm robustness.

To account for the nested data structure arising from multiple ROIs per patient, we performed three complementary analyses. First, within-patient reproducibility was evaluated by pairwise Pearson correlations of cell-type and cellular neighborhood proportion profiles, stratified as intrapatient versus interpatient pairs. Second, sensitivity analyses were performed using linear mixed-effects models (R package lmerTest) fitted as proportion ~site + (1 | patient), with tissue site (BC vs BrM) as a fixed effect and patient as a random intercept.[52] This framework partitions variance into between-patient and within-patient components and provides site effect estimates with appropriately adjusted SEs, as recommended for multiplexed spatial proteomics data with multiple ROIs per sample.[53] Third, patient-level paired comparisons were performed for the five patients with matched BC-BrM samples by averaging per-ROI proportions within each site and applying paired Wilcoxon tests.

Author affiliations
[1]Department of Breast Surgery, Zhujiang Hospital, Southern Medical University, Guangzhou, Guangdong, China
[2]Guangdong Cardiovascular Institute, Guangdong Provincial People's Hospital, Guangdong Academy of Medical Sciences, Guangzhou, China
[3]Guangdong Provincial Biomedical Engineering Technology Research Center for Cardiovascular Disease, Zhujiang Hospital, Guangzhou, Guangdong, China
[4]Chinese Institutes for Medical Research, Beijing, China
[5]Department of Breast Cancer, Cancer Centre, Guangdong Provincial People's Hospital (Guangdong Academy of Medical Sciences), Southern Medical University, Guangzhou, China

Acknowledgements We would like to acknowledge and thank the patients involved in this study for their participation.

Contributors JZ and JY performed the research and wrote the manuscript. YM and ZL performed the analysis. YW wrote the manuscript with input from all other authors. JS reviewed the manuscript. MY acquired funding for the study. All authors reviewed and revised the manuscript. MY is the guarantor of this work.

Funding This work was supported by the National Natural Science Foundation of China (grant no. 82373427 and 82072939 to MY), the Guangzhou Science and Technology Program key projects (grant no. 202206010110 to MY), the Guangdong Basic and Applied Basic Research Foundation (grant no. 2022A1515010425 to MY), the WU JIEPING Medical Foundation,WJPMF (grant no. 320.6750.2024-21-131 to MY), and the Beijing Natural Science Foundation (grant no. L2510026 and L234002 to JS).

Competing interests None declared.

Patient consent for publication Not applicable.

Ethics approval Ethics approval for this study was granted by the Institutional Ethics Committee of Guangdong Provincial People's Hospital (approval no. S2024-1254-01). Participants gave informed consent to participate in the study before taking part.

Provenance and peer review Not commissioned; externally peer reviewed.

Data availability statement Data are available upon reasonable request. The data generated in this study are available from the corresponding author upon reasonable request, subject to institutional and ethical regulations.

ORCID iD

Jianpeng Sheng https://orcid.org/0000-0003-3262-2587

REFERENCES

1 Siegel RL, Giaquinto AN, Jemal A. Cancer statistics, 2024. *CA A Cancer J Clinicians* 2024;74:12–49.
2 Sung H, Ferlay J, Siegel RL, *et al*. Global Cancer Statistics 2020: GLOBOCAN Estimates of Incidence and Mortality Worldwide for 36 Cancers in 185 Countries. *CA Cancer J Clin* 2021;71:209–49.
3 Kuett L, Bollhagen A, Tietscher S, *et al*. Distant Metastases of Breast Cancer Resemble Primary Tumors in Cancer Cell Composition but Differ in Immune Cell Phenotypes. *Cancer Res* 2025;85:15–31.
4 Kanchan RK, Siddiqui JA, Mahapatra S, *et al*. microRNAs Orchestrate Pathophysiology of Breast Cancer Brain Metastasis: Advances in Therapy. *Mol Cancer* 2020;19:29.
5 Sammons SL, Sanglier T, Leone JP, *et al*. Prevalence by therapy line and incidence of breast cancer brain metastases in 18075 patients. *J Natl Cancer Inst* 2025;117:1565–72.
6 Raghavendra AS, Ibrahim NK. Breast Cancer Brain Metastasis: A Comprehensive Review. *JCO Oncol Pract* 2024;20:1348–59.
7 Eichler AF, Kuter I, Ryan P, *et al*. Survival in patients with brain metastases from breast cancer. *Cancer* 2008;112:2359–67.
8 Fares J, Ulasov I, Timashev P, *et al*. Emerging principles of brain immunology and immune checkpoint blockade in brain metastases. *Brain* 2021;144:1046–66.
9 Khan IM, Khan SU, Sala HSS, *et al*. TME-targeted approaches of brain metastases and its clinical therapeutic evidence. *Front Immunol* 2023;14:14–2023.
10 Li T, Sun S, Li Y, *et al*. Immunotherapy revolutionizing brain metastatic cancer treatment: personalized strategies for transformative outcomes. *Front Immunol* 2024;15:1418580.
11 Zhao N, Rosen JM. Breast cancer heterogeneity through the lens of single-cell analysis and spatial pathologies. *Semin Cancer Biol* 2022;82:3–10.
12 Liu K, Han H, Xiong K, *et al*. Single-cell landscape of intratumoral heterogeneity and tumor microenvironment remolding in pre-nodal metastases of breast cancer. *J Transl Med* 2024;22:804.
13 Karimi E, Yu MW, Maritan SM, *et al*. Single-cell spatial immune landscapes of primary and metastatic brain tumours. *Nature* 2023;614:555–63.
14 Angelo M, Bendall SC, Finck R, *et al*. Multiplexed ion beam imaging of human breast tumors. *Nat Med* 2014;20:436–42.
15 Williams CG, Lee HJ, Asatsuma T, *et al*. An introduction to spatial transcriptomics for biomedical research. *Genome Med* 2022;14:68.
16 Liu L, Chen A, Li Y, *et al*. Spatiotemporal omics for biology and medicine. *Cell* 2024;187:4488–519.
17 Danenberg E, Bardwell H, Zanotelli VRT, *et al*. Breast tumor microenvironment structures are associated with genomic features and clinical outcome. *Nat Genet* 2022;54:660–9.
18 Eng JR, Bucher E, Hu Z, *et al*. Highly multiplexed imaging reveals prognostic immune and stromal spatial biomarkers in breast cancer. *JCI Insight* 2025;10:e176749.
19 Zhao YX, Song JY, Bao XW, *et al*. Single-cell RNA sequencing-guided fate-mapping toolkit delineates the contribution of yolk sac erythro-myeloid progenitors. *Cell Rep* 2023;42:113364.
20 Tang J, Sheng J, Zhang Q, *et al*. Runx3-overexpression cooperates with ex vivo AKT inhibition to generate receptor-engineered T cells with better persistence, tumor-residency, and antitumor ability. *J Immunother Cancer* 2023;11:e006119.
21 Crouch EE, Doetsch F. FACS isolation of endothelial cells and pericytes from mouse brain microregions. *Nat Protoc* 2018;13:738–51.
22 Mitsuhashi A, Koyama K, Ogino H, *et al*. Clock pathway inhibitor overcomes tumor immune-exclusion via regulation of fibrocyte differentiation. *NPJ Precis Oncol* 2025;9:274.
23 Schulz M, Michels B, Niesel K, *et al*. Cellular and Molecular Changes of Brain Metastases-Associated Myeloid Cells during Disease Progression and Therapeutic Response. *iScience* 2020;23:101178.
24 Katoh H, Okamoto R, Yokota M, *et al*. CD163$^+$ Tumor-Associated Macrophage Recruitment Predicts Papillary Thyroid Cancer Recurrence. *J Surg Res* 2024;303:532–44.
25 Matsubara E, Komohara Y, Shinchi Y, *et al*. CD163-positive cancer cells are a predictor of a worse clinical course in lung adenocarcinoma. *Pathol Int* 2021;71:666–73.
26 Van Swearingen AED, Lee MR, Rogers LW, *et al*. Genomic and immune profiling of breast cancer brain metastases. *Acta Neuropathol Commun* 2025;13:99.
27 Dong W, Sheng J, Cui JZM, *et al*. Systems immunology insights into brain metastasis. *Trends Immunol* 2024;45:903–16.
28 Klughammer J, Abravanel DL, Segerstolpe Å, *et al*. A multi-modal single-cell and spatial expression map of metastatic breast cancer biopsies across clinicopathological features. *Nat Med* 2024;30:3236–49.
29 Hsieh W-C, Budiarto BR, Wang Y-F, *et al*. Spatial multi-omics analyses of the tumor immune microenvironment. *J Biomed Sci* 2022;29:96.
30 Xie J, Yang A, Liu Q, *et al*. Single-cell RNA sequencing elucidated the landscape of breast cancer brain metastases and identified ILF2 as a potential therapeutic target. *Cell Prolif* 2024;57:e13697.
31 Cheng S, Li Z, Gao R, *et al*. A pan-cancer single-cell transcriptional atlas of tumor infiltrating myeloid cells. *Cell* 2021;184:792–809.
32 Zhang Y, Zhong F, Liu L. Single-cell transcriptional atlas of tumor-associated macrophages in breast cancer. *Breast Cancer Res* 2024;26:129.
33 Chen S, Cui W, Chi Z, *et al*. Tumor-associated macrophages are shaped by intratumoral high potassium via Kir2.1. *Cell Metab* 2022;34:1843–59.
34 Klemm F, Maas RR, Bowman RL, *et al*. Interrogation of the Microenvironmental Landscape in Brain Tumors Reveals Disease-Specific Alterations of Immune Cells. *Cell* 2020;181:1643–60.
35 Zhang Q, Abdo R, Iosef C, *et al*. The spatial transcriptomic landscape of non-small cell lung cancer brain metastasis. *Nat Commun* 2022;13:5983.
36 Myers KV, Amend SR, Pienta KJ. Targeting Tyro3, Axl and MerTK (TAM receptors): implications for macrophages in the tumor microenvironment. *Mol Cancer* 2019;18:94.
37 McCracken MN, Cha AC, Weissman IL. Molecular Pathways: Activating T Cells after Cancer Cell Phagocytosis from Blockade of CD47 “Don’t Eat Me” Signals. *Clinical Cancer Research* 2015;21:3597–601.
38 Lauwers Y, De Groof TWM, Vincke C, *et al*. Imaging of tumor-associated macrophage dynamics during immunotherapy using a CD163-specific nanobody-based immunotracer. *Proc Natl Acad Sci U S A* 2024;121:e2409668121.
39 Wischnewski V, Guerrero Aruffo P, Massara M, *et al*. The local microenvironment suppresses the synergy between irradiation and anti-PD1 therapy in breast-to-brain metastasis. *Cell Rep* 2025;44:115427.
40 Su Y-T, Butler M, Zhang M, *et al*. MerTK inhibition decreases immune suppressive glioblastoma-associated macrophages and neoangiogenesis in glioblastoma microenvironment. *Neurooncol Adv* 2020;2:vdaa065.
41 Raphael I, Kumar R, McCarl LH, *et al*. TIGIT and PD-1 Immune Checkpoint Pathways Are Associated With Patient Outcome and Anti-Tumor Immunity in Glioblastoma. *Front Immunol* 2021;12:637146.
42 Wu C, Zhang G, Wang L, *et al*. Spatial proteomic profiling elucidates immune determinants of neoadjuvant chemo-immunotherapy in esophageal squamous cell carcinoma. *Oncogene* 2024;43:2751–67.
43 Chevrier S, Crowell HL, Zanotelli VRT, *et al*. Compensation of Signal Spillover in Suspension and Imaging Mass Cytometry. *Cell Syst* 2018;6:612–20.
44 Ruan J, Li Q, Jin Y, *et al*. Multiple-omics analysis reveals a dedifferentiation-immune loop in intrahepatic cholangiocarcinoma. *Mol Ther* 2025;33:1803–24.
45 Stuart T, Butler A, Hoffman P, *et al*. Comprehensive Integration of Single-Cell Data. *Cell* 2019;177:1888–902.
46 Ma Y, Zhou X. Spatially informed cell-type deconvolution for spatial transcriptomics. *Nat Biotechnol* 2022;40:1349–59.
47 Schürch CM, Bhate SS, Barlow GL, *et al*. Coordinated Cellular Neighborhoods Orchestrate Antitumoral Immunity at the Colorectal Cancer Invasive Front. *Cell* 2020;182:1341–59.
48 Cable DM, Murray E, Zou LS, *et al*. Robust decomposition of cell type mixtures in spatial transcriptomics. *Nat Biotechnol* 2022;40:517–26.

49 Jin S, Guerrero-Juarez CF, Zhang L, *et al*. Inference and analysis of cell-cell communication using CellChat. *Nat Commun* 2021;12:1088.
50 Zhang J, Song J, Tang S, *et al*. Multi-omics analysis reveals the chemoresistance mechanism of proliferating tissue-resident macrophages in PDAC via metabolic adaptation. *Cell Rep* 2023;42:112620.
51 Aibar S, González-Blas CB, Moerman T, *et al*. SCENIC: single-cell regulatory network inference and clustering. *Nat Methods* 2017;14:1083–6.
52 Kuznetsova A, Brockhoff PB, Christensen RHB. lmerTest Package: Tests in Linear Mixed Effects Models . *J Stat Soft* 2017;82.
53 Samorodnitsky S, Wu MC. Statistical analysis of multiple regions-of-interest in multiplexed spatial proteomics data. *Brief Bioinform* 2024;25:bbae522.